# An Automated Optical Liquid Film Thickness Measurement Method

T. A. Shedd and T. A. Newell

ACRC TR-134 December 1997

*For additional information:*

Air Conditioning and Refrigeration Center
University of Illinois
Mechanical & Industrial Engineering Dept.
1206 West Green Street
Urbana, IL 61801

(217) 333-3115

*Prepared as part of ACRC Project 77*
*Experimental Investigation of Refrigerant/Oil Flows*
*Using an Ambient Pressure, Flow Visualization Facility*
*T. A. Newell, Principal Investigator*

*The Air Conditioning and Refrigeration Center was founded in 1988 with a grant from the estate of Richard W. Kritzer, the founder of Peerless of America Inc. A State of Illinois Technology Challenge Grant helped build the laboratory facilities. The ACRC receives continuing support from the Richard W. Kritzer Endowment and the National Science Foundation. The following organizations have also become sponsors of the Center.*

Amana Refrigeration, Inc.
Brazeway, Inc.
Carrier Corporation
Caterpillar, Inc.
Copeland Corporation
Dayton Thermal Products
Delphi Harrison Thermal Systems
Eaton Corporation
Ford Motor Company
Frigidaire Company
General Electric Company
Hydro Aluminum Adrian, Inc.
Indiana Tube Corporation
Lennox International, Inc.
Modine Manufacturing Co.
Peerless of America, Inc.
Redwood Microsystems, Inc.
The Trane Company
Whirlpool Corporation
York International, Inc.

*For additional information:*

*Air Conditioning & Refrigeration Center*
*Mechanical & Industrial Engineering Dept.*
*University of Illinois*
*1206 West Green Street*
*Urbana IL 61801*

*217 333 3115*

# AN AUTOMATED OPTICAL LIQUID FILM THICKNESS MEASUREMENT METHOD

Timothy Allen Shedd, MS
Department of Mechanical and Industrial Engineering
University of Illinois at Urbana-Champaign
Professor Ty A. Newell, Advisor

## Abstract

The need to measure the thickness of thin liquid films is evident from the number of methods that have been developed to do so. Many of these methods have significant drawbacks, such as intrusive probes or the dependence on a conductive liquid. A non-intrusive, automated, optical film thickness measurement technique has been developed to be used with a wide range of fluids and with virtually any flow configuration. In this method, light is reflected from the surface of a liquid film flowing over a transparent wall. This reflected light generates an image on the outside of the wall which is captured and digitized using a CCD camera and framegrabber card in a desktop computer. The image is processed to determine the positions of the reflected light rays, with which the film thickness and film slope are calculated. The entire process is automated and can be performed in less than 9 seconds on a 486 PC, allowing many data points to be collected efficiently. Film thicknesses as small as 0.03 mm can be determined using inexpensive components, with the possibility of greater precision using more advanced imaging equipment. An automated calibration procedure allows for the determination of the necessary physical parameters automatically, so the index of refraction of the test fluid or the test section wall need not be known a-priori. A prototype of the automated system generates static liquid measurements that agree to within 3% of measurements made using the needle-contact method. Film thickness data are also presented for an air-water system in cylindrical, annular, two-phase flow and compared with data from the literature.

# Contents

# List of Figures

# List of Tables

# Definitions of Symbols Used

$\alpha, \beta$ Dummy angles

$\eta_{pix}$ Pixel deviation coefficient

$\Omega$ Spatial frequency

$\phi$ Slope angle of the film surface

$\sigma$ Standard deviation of pixels along processed reflected light ring edge

$\theta$ Angle between incident ray and interface normal used in Fresnel relations

$\theta_1$ Angle between ray approaching the interface and the normal to the interface

$\theta_2$ Angle between ray leaving the interface and the normal to the interface

$\theta_c$ Critical angle

$\theta_{cl}$ Critical angle of liquid-air interface

$\theta_{cw}$ Critical angle of wall-air interface

$\theta_{cwl}$ Critical angle of wall-liquid interface

$\theta_{l1}$ Angle of ray entering liquid

$\theta_{l2}$ Angle of ray leaving liquid

$\theta_{lw}$ Angle of ray entering the liquid from the wall

$\theta_{w1}$ Angle between ray approaching wall-liquid interface and the interface normal

$\theta_{w2}$ Angle between ray leaving wall-liquid interface and the interface normal

$\theta_{wl}$ Angle of ray entering the wall from the liquid

$\theta_{wv}$ Angle of ray entering the wall from the vapor

$\theta_{vw}$ Angle of ray entering the vapor from the wall

$C$ Confidence value

$d_{src}$ Distance between light sources

$D_i$ Dummy sum variable

$E_o$ Electric field intensity of ray leaving interface

$E_i$ Electric field intensity of ray incident to interface

$F$ Discrete, two-dimensional filter

$\widehat{F}(\Omega)$ Fourier transform of $F$

$g(i), h(i)$ Components of a separable filter

$I$ An $n \times m$ section of the image

$\widehat{I}(\Omega)$ Fourier transform of $I$

$i, j$ Convolution sum indices

$k$ Discrete pixel index

$\dot{m}_a$ Mass flow rate of air

$\dot{m}_l$ Mass flow rate of liquid

$n, m$ Width and Height of a convolution mask

$n$ Ratio of indices of refraction, $n_2/n_1$

$n_1$ Index of refraction of medium 1

$n_2$ Index of refraction of medium 2

$N$ Number of pixels in calculation of average

$N$ Number of discrete points in convolution sum

$p_L$ Pixel location of reflected light ring from left source

$p_R$ Pixel location of reflected light ring from right source

$P(x, y)$ Result of a 2-D convolution

$\widehat{P}(\Omega)$ Fourier transform of $P$

$P_o$ Power of ray leaving interface

$P_i$ Power of ray incident to interface

$p_{scale}$ Pixel scale factor

$r_{TE}$ Transverse electric Fresnel reflection coefficient, $E_o/E_i$

$r_{TM}$ Transverse magnetic Fresnel reflection coefficient, $E_o/E_i$

$R_{avg}$ Average reflectivity

$t_l$ Thickness of liquid film

$t_L$ Thickness of the film at reflection from left source

$t_R$ Thickness of the film at reflection from right source

$t_{tl}$ Liquid transition thickness: Thickness at which the light reflected from the wall-liquid interface generates a light ring smaller than the ring of light reflected from the liquid surface

$t_w$ Thickness of wall

$T_{avg}$ Average transmissivity

$W$ Pixel width of image

$x$ Total distance between the light source and the ring of light reflected from the liquid surface

$\overline{x}$ Mean pixel location along processed reflected light ring edge

$x_o$ Location of the reflected light ring when no liquid is present

$x_{dry}$ Linear distance traversed by the light ray as it travels through the wall from the source to the liquid, then from the liquid interface to the wall surface

$x_{fld}$ Total linear distance traversed by the light reflected from the wall-liquid interface with a thick layer of liquid present

$x_l$ Linear distance traversed by the light ray as it travels through the liquid layer

$x_{liq}$ Total linear distance traversed by the light reflected from the liquid surface

$x_{pix}$ Location of a given edge pixel

$x_r$ Distance between surface reflection points

$x_{ref}$ Location of the point at which the first fully reflected ray returns to the outer wall surface, as determined by weighted averages

$x_{w1}$ Linear distance traversed by ray from source to liquid interface

$x_{w2}$ Linear distance traversed by ray from the liquid interface to the outer wall surface

# Chapter 1

# Introduction

Thin liquid films occur very often in engineering applications with thicknesses that may range from below 10 microns ($10^{-6}$m) to about 5 mm. For instance, during the operation of a fuel delivery system for an internal combustion engine, a thin film of fuel forms along the walls of the combustion cylinder, and its distribution and composition are important in determining the outcome of the combustion process. Thin films are also present when a gas or vapor and a liquid flow through a pipe together. This is known as a two-phase flow since both a vapor phase and a liquid phase of the fluid or fluid mixture are moving through the pipe together.

Two-phase flow is a complicated and not completely understood process. Understanding it is of extreme importance, however, to such applications as nuclear power generation, steam power generation, crude oil delivery and refinement, chemical processing, and refrigeration systems. One of the most important parameters in modeling two-phase flow is the distribution of the liquid layer. Beginning in the early 1960's, investigators began developing methods for measuring this liquid film thickness in flows associated with steam generation in a nuclear power plant. Here it is critical for safe operation that the liquid layer be present, and for plant efficiency studies, a detailed knowledge of the liquid-vapor flow is needed. As a result, many of the film measurement systems have been developed for use with water, taking advantage of its electrical properties. Different methods became necessary as attention was given to other fluids, such as those in oil or chemical processing flows.

The method discussed in this work is an inexpensive, non-intrusive measurement system for use with most fluids of interest. Total internal reflection

of light is used to create an image of the fluid surface on the outside of the wall carrying the flow. This image is then acquired, digitized and processed using custom software to produce a film height that is accurate to within 0.03 mm. This method can be used to measure films ranging from below 0.1 mm to a thickness approximately equal to the thickness of the wall supporting the flow (generally 3 to 5 mm). The measurement apparatus can be moved quickly and easily to virtually any point in the flow. In addition, the system is computer controlled and operated, allowing for the measurement of large numbers of data points in a short time.

The purpose of this work, then, is to present in detail the development and operation of this new measurement system. To begin, a brief survey of film thickness measurement methods is presented in Chapter 2. The theory behind the operation of the new, automated system is then described in Chapter 3, followed by a description of the calibration procedure in Chapter 4. Chapter 5 presents data validating the operation of the system and the calibration procedure using film thickness data collected from both static film conditions and from conditions in an air-water two-phase flow loop. To conclude, Chapter 6 summarizes the current work and presents possibilities for application of the measurement technique to other fluid situations.

# Chapter 2

# Survey of Film Thickness Measurement Methods

## 2.1 The Needle-Contact Method

One of the earliest and most straightforward methods used in the measurement of thin liquid films is the needle-contact method. Several investigators have employed this method, which is based on the conductivity of water (Dallman; 1978; Laurinat; 1982; Hewitt; 1982; Sekoguchi et al.; 1982; Fukano and Ousaka; 1989). A test rig is fabricated that allows a needle (or thin wire) to be lowered or raised with a micrometer. The needle is very thin (on the order of 0.3 mm) and is coated with an insulating material except at the tip. An electrode is mounted in the wall opposite the needle assembly so that when the needle touches the water film, a closed circuit is formed. This entire apparatus is constructed so that the test section tubes can be inserted into the ends of the test rig, with the inner surfaces of the test section and test rig flush, minimizing any flow disruptions. The needle assembly may be rotated to obtain measurements at different circumferential locations.

While of limited mobility, film thicknesses can be measured from below 0.1 mm to essentially the diameter of the test section. Due to the wavy structure of the film surface, statistical methods must be applied to determine the average film thickness. One such analysis is given by Sekoguchi et al. (1975). In addition, care must be taken to compensate for thermal expansion of the needle and the bridging effect of drops that may form on the needle tip.

Due to its simplicity and its physically intuitive operation, the needle-

contact method is often used as a standard measurement with which other methods are compared. Limiting errors have been associated with the mechanical positioning apparatus (Coney et al.; 1989). In addition, it seems that the electrical signal generated by the devices in the literature may not accurately portray the high and low peaks in the actual film thickness variations of rapidly moving, wavy films, though average film thicknesses generated from these electrical traces appear accurate.

## 2.2 Electrical Conductance Methods

Of all the film thickness measurement methods, perhaps the electrical conductance method is the most used. Conceptually quite simple, this method uses the fact that water conducts electricity reasonably well. Theoretically, if two bare, parallel wires are in contact with water, the amount of current that flows between them will be directly proportional to the depth of liquid that is in contact with the wires. An alternating current supply is generally used to aid in eliminating noise and to slow the deterioration of the electrodes. Some of the early investigators developed the necessary electromagnetic theory and optimum probe configurations (Miya; 1970; Coney; 1973; Brown et al.; 1978; Dallman; 1978; Villeneuve and Ouellet; 1978). These early works determined that frequencies of 10 kHz or greater should be used for the probe signal, and that, within reason, higher frequencies provided better sensitivities. Although the theory predicted a linear response with film height, nonlinearities and the nature of the system required regular calibration if results with better than 10% accuracy were desired. In addition, it was determined that the parallel wire conductance method had a lower limit of about 0.5 mm, due in large part to the significant contributions of the capillary rise of the liquid on the electrodes.

Building on the earlier work, the parallel wire technique was refined and more advanced signal conditioning circuitry was developed (Laurinat; 1979, 1982; Andritsos; 1985; Azzopardi; 1986; Bousman et al.; 1996). Most of these methods used a test apparatus that had probe locations machined at some regular interval radially about the test section (every 30° or 45°, for example) into which a plug containing the probes could be inserted.

Among recent implementations of this method, signal frequencies of 10 kHz (Bousman et al.; 1996), 21 kHz (Jayanti et al.; 1990) and 25 kHz (Karapantsios et al.; 1989) have been used. Jayanti et al. used their probes over a range of 0.2 – 3 mm, while Bousman et al., extended the range to 0.2 – 6 mm. Bousman et al., claim an uncertainty of 0.02 mm as do Karapantsios et al., though the latter only used their probes on films greater than 0.5 mm. Karapantsios et al., estimated their probe sensitivity to be quite good at 0.002 mm and very linear above film heights of 0.5 mm.

One significant variation of this method is to use flush mounted electrodes rather than the intrusive parallel wires. This method is developed and employed by Andritsos (1985) and Hagiwara et al. (1982, 1989).

Though so widely used, conductance probes leave much to be desired. First, the parallel wire probes are intrusive, and actually subject to damage from the flow itself (Laurinat; 1982). They must be calibrated frequently (Andritsos; 1985), as must the probe signal analyzer and the fluid under test (Laurinat; 1979). The flush mounted probe is even more difficult to calibrate according to Andritsos. In addition, although the probes may be placed in several different circumferential locations, it is difficult or impossible to move the test rig along the test section. Additional test rigs are required at each location were film thickness is desired.

Finally, these probes are calibrated using static films and needle-contact data, or using vertically falling films. In either case, the liquid is generally smooth and most likely does not contain any entrained vapor bubbles. However, in horizontal, annular flow, the surface is generally not smooth, and the flow contains many vapor bubbles (Hewitt et al.; 1990). Sharp variations in film height between probes are possible, with the conductance reading reflecting the thinnest film and not necessarily an average thickness. In addition, bubbles in the flow will have a dramatic impact on the measured conductance, particularly in thin films. Thus, it seems that these methods may not be very accurate for very thin films (say, $< 0.2$ mm).

## 2.3 Capacitance Methods

Electrical capacitance measurements have attracted much interest throughout a long history of development (Özgü and Chen; 1973; Sun et al.; 1981; Sundaram et al.; 1981; Turko et al.; 1981; Hewitt; 1982; Chun and Sung; 1986; Klug and Mayinger; 1994; Chen et al.; 1996; Thorncroft and Klausner; 1997). This interest is due in large part to the fact that capacitance can be measured on non-conducting fluids, eliminating one of the significant constraints of the needle-contact and conductance methods. To summarize these many efforts, an alternating current signal is applied between two electrodes and the capacitance (or admittance) of the test circuit is determined. Using well-known electromagnetic field theory along with the geometry of the test section, a relation is developed for film thickness (or void fraction) versus measured capacitance. Some geometries follow the theory better than others; less predictable designs require the generation of a calibration curve for the fluid under test.

The volume of work focused on capacitance methods results from the variety of possible electrode configurations and test section geometries. In round tubes, radial capacitors can be employed with one electrode in the center of the test section and the other on the outside. Most are less intrusive, consisting of parallel rectangular electrodes, pairs of circular electrodes, or concentric circular electrodes mounted in the test section wall. Film thicknesses have been documented by capacitance measurements from about 0.5 mm to about 5 mm.

While popular, capacitance methods are beset with several challenges. One is the fact that after a certain film height, the capacitance value generated becomes essentially constant for a given set of electrodes. To compensate for this, the electrode spacing can be changed, but with a subsequent loss in sensitivity. Thus, the ability to measure a wide range of film thicknesses is limited. Great care must be taken to compensate for leakage currents that will occur if electrodes are in contact with the test fluid. In addition, the capacitance of a fluid can be affected by its temperature, and this must be accounted for (Klausner et al.; 1992).

Measuring capacitance accurately is a challenging procedure in itself, particularly with capacitance changes on the order of picofarads or less indicating

significant changes in film thickness. Contacts and leads must be carefully shielded to eliminate stray capacitances and interference from other sources, and the measurement frequency should be chosen with some care.

## 2.4 Microwave Absorption

Though limited essentially to the measurement of symmetrical annular flow in two-phase liquid down-flow conditions, the use of microwave absorption can be used to generate precise film thickness data from about 0.4 mm to at least 1 mm (Roy et al.; 1986). A special microwave waveguide is constructed which allows the flow to pass through a Plexiglas test section at its center. Microwave energy at 1.22 GHz is applied to one end of the waveguide and a detector on the other end is used to determine how much energy is absorbed in the test section. A linear calibration curve can be generated allowing for very precise measurements within the range of calibration.

In addition to its rather small range of application, the operation of this unit requires some knowledge of microwave systems. The special test section is also semi-permanent, further limiting the flexibility of its operation.

## 2.5 Laser Induced Fluorescence

Laser induced fluorescence (LIF) can provide very detailed and accurate information about the liquid film layer. In operation, light from an intense source, e.g. a mercury vapor lamp (Hewitt; 1982) or an argon-ion laser (Schmitt et al.; 1982; Driscoll et al.; 1992), is focused into the liquid film which carries a fluorescent dye. Some percentage of this light is absorbed, causing dye molecules to fluoresce. The power of this fluorescent light can be theoretically determined as a function of the number of dye molecules in the light path. Thus, for a given dye mixture, a calibration curve can be obtained relating film thickness (or the volume of liquid-dye mixture exposed to the light) to the fluorescent light power.

Hewitt describes early efforts in which the mercury vapor source is used with a sodium fluorescein dye to measure film thicknesses in a closed pipe. Through the use of relatively simple optics, the light is introduced through

a transparent pipe section and the fluorescent light is gathered, along with reflected light, and analyzed. Because the dye will emit light over a very narrow band of wavelengths, the dye signal can be separated from the reflected light using optical filters or a spectrometer. In addition, since the light from the source is focused into the liquid layer at the near wall, the signal generated will not be affected by the fact that a film surrounds the interior of the pipe.

Driscoll and Schmitt et al. use a laser source to study the film thickness on an open surface. They have refined the technique considerably, taking into account film surface slope and other effects. Using translating optics, they have been able to obtain detailed film topologies with film thickness sensitivities on the order of 0.01 mm and spatial resolutions of 0.04 mm. Very thick films ( $>$ 10 mm) can be measured as well with similar sensitivities.

This method may be one of the few available that can provide such detailed and nearly instantaneous liquid film information. In implementation, care must be taken to ensure stability of the light source with respect to the fluid test section. Driscoll and Schmitt et al. conducted their studies on a vibration-isolated optical breadboard. The response of the fluid must be calibrated with each use, though once calibrated, excellent repeatability can be attained. The system currently requires the use of a rather expensive light source, though laser prices have been decreasing steadily. Finally, the measurements are limited to situations where fluids can be impregnated with the fluorescent dye, which may significantly limit the number of liquids that can be studied.

## 2.6 Light Absorption

Light passing through a liquid will be absorbed to some degree; the amount of absorption is a volumetric property of the liquid. If, then, light is directed through a liquid film and detected by a sensor opposite the source, fluctuations in the light intensity received by the sensor can be correlated to film thickness.

Barter and Lee (1994) have used this characteristic to generate information about surface waves on a fluid layer. A red laser diode generates uniform light which is spread out by a lens system to illuminate a region about 3 cm wide. The light is collected by a lens system after passing through the liquid

and is focused onto a photodiode array which is sampled at 37.5 kHz. This, then, provides a nearly continuous display of the film surface structure within the illuminated region. A green dye is added to the water to increase the absorption coefficient for the red light.

A very similar approach is taken by Sattelmayer et al. (1987). To compensate for changes in the fluid composition, temperature and possible fouling of the optical surfaces, a calibration cell receives a continuous flow of the fluid under test. The thickness of the fluid in the calibration cell is set at 1 mm. Data is taken simultaneously from both the flow test section and the calibration cell and each data point from the test section is calibrated using information from the calibration cell. These investigators used focused light to study the time variation of a very small spatial area. Excellent data are presented for a variety of fluids with sensitivities of better than 0.005 mm.

An additional technique uses light from two different sources simultaneously (Himmelsbach et al.; 1994; Müller et al.; 1994). Red light (633 nm) and infrared light (1523 nm) is focused onto the liquid. Fiber optics positioned in the pipe wall opposite the light sources receive the light through the liquid and transmit it to sensors. The infrared light is absorbed to a much greater extent than the red light. Thus, the red light serves to calibrate the infrared readings to light reflected from the fluid surface and light lost to fouling of the optical components. Measurements of films from about 0.025 mm to about 0.1 mm are obtained with certainties of about 0.005 mm.

Primary concerns with this technique are the stability of the light source with respect to the test section and compensation for surface reflections. The last two approaches discussed are not so prone to vibrational instabilities because light signals are delivered and received through optical fibers mounted either flush with the test section wall or projecting through the wall. This greatly complicates the test section construction and, of course, any projection will potentially disturb the flow being examined. Only the last method attempts to compensate for surface reflections which can be quite significant if the slope of the surface becomes large.

## 2.7 Interferometry

Extremely thin liquid films can form in certain situations which can be measured through interferometry. One such instance is the non-equilibrium condensation of vapor that may occur in two-phase flow, combustion and other situations. To study this, Maerfat et al. (1989) have measured the condensation of a thin liquid film at the bottom of a shock tube using interferometry.

Interferometry is based on the principle that light is reflected each time it passes from one material to another. The amount of light reflected depends on the wavelength of the light and the angle with which the light reaches the interface between the two materials. This has been frequently put to use to create mirrors or filters of several thin coatings of different materials that reflect a narrow band of wavelengths very strongly, while all other wavelengths of light pass through.

In this case, the layers consist of air, a very thin (10 nm) naturally adsorbed film, optical glass, the thin liquid film of interest and the surrounding vapor. The investigators have developed a simplified model for the interaction of red (632.8 nm) light with these layers which predicts the amount of light reflected as the liquid layer changes from 0 to 250 nm (0.00025 mm). Because the reflectance is periodic as the liquid layer increases beyond this thickness, this method is not useful for thicker films.

## 2.8 External Reflection of Light

The reflection of light from liquid surfaces has been used to determine not only film thickness, but also the slope of the liquid surface. Coney et al. (1989) have developed a method in which two laser beams are directed toward the liquid surface, one normal to the liquid-carrying wall and one at an angle to it. Using a series of mirrors, the reflections of these beams are brought to fall on a single screen, and these no-liquid positions are marked as references. As liquid flows across the surface, the positions of the two reflection points move and are recorded with a movie camera. The recorded images can then be analyzed and the liquid height and surface slope at the test point can be determined from the positions of the reflected light spots with respect to the

reference marks. Measurements have been taken of films in the 0.5 mm to 2 mm thickness range with a precision of 0.01 mm and an accuracy of 4% when compared with needle-contact measurements. The method may be used with any fluid, regardless of composition or optical properties.

Stability of the laser sources, mirrors and output screen with respect to the test surfaces are of extreme importance. For this reason, the entire experiment is carried out on a vibration-dampening optical breadboard. While this method is intended for use on a flat, open surface, it is possible that it could be adapted for use on curved surfaces with known geometries or even in a transparent, enclosed pipe, provided the upper surface of the pipe remains clear of any liquid.

## 2.9 Total Internal Reflection of Light

When light travels through one substance into another, some of the light will be reflected at the interface, while the remainder will pass through to the second substance, but bent at an angle in accordance with Snell's law. At a certain angle, the critical angle, the light that would have passed on through will be bent such that it is all reflected back into the first substance. This is called total internal reflection of light (TIR). TIR can be used to determine the height of a liquid film flowing in a transparent pipe or on a transparent surface.

Than et al. (1993) and Yu et al. (1996) have developed some theory based on delivering light to the liquid through the test section wall with an optical fiber, and receiving the light reflected from the liquid surface through other optical fibers also embedded in the wall. The methods presented are nearly identical, though Yu et al. allow for a 2-dimensional sloping surface while Than et al. assume a uniform 1-dimensional slope. In both methods, laser light is directed to the fluid through a fiber surrounded by collecting fibers which are in turn connected to sensors and analyzing electronics. While the analysis in these methods is good, the suggested implementations would be practical only for extremely thin films due to the small dimensions of the receiving fibers. In addition, the analysis assumes ideal laser beam profiles and intensity distributions. No attempt is made to compensate for absorption

in the liquid, uneven fouling or wear of the optical surfaces, or the non-linear nature of the signal generated by the receiving sensors.

A similar, but more practical implementation is presented by Evers and Jackson (1995). Here, laser light is transmitted to the liquid through the solid surface wall via fibers surrounding a bundle of collecting fibers. The light received by the center fibers is detected by a photodiode whose output is processed and recorded. Due to the nonlinear behavior of both the photodiode and the reflected light, calibration curves must be generated for each fluid of interest. Results for fluids such as water, milk, motor oil and Stoddard fluid are presented, indicating the appropriate measurement range to be from about 0.25 mm to about 2 mm, though saturation of the photodiode signal occurs at different thicknesses for each liquid and sets the limit on the maximum thickness that may be accurately measured. Calibration should be performed regularly to account for alterations of the optical surfaces and the temperature of the photodiode.

Each of the above methods require the permanent mounting of a fiber assembly in a test section or surface. This places significant restrictions on the use of these methods in analyzing complex flow situations, as well as complicating the construction of test sections that will not disturb the fluid flow.

A novel optical technique has been presented that also uses the total internal reflection of light rays to measure the height of liquid films (Hurlburt and Newell; 1996). This method offers many advantages over other measurement techniques: It is non-intrusive; no permanent mounting is required so data can be acquired at any point of a clear test section; any liquid can be measured; no calibration is required since the method is a direct measurement of a signal that is a linear function of the film height; and it is relatively inexpensive and easy to construct.

With this technique, a light source, such as a light emitting diode (LED), is placed on the outside of a transparent wall. A thin, opaque coating on the wall spreads the light out and serves as a screen to display the image of light reflected back from the liquid surface, forming a ring around the light source. The radius of this ring at any point is directly proportional to the height of the liquid film flowing past. Thus, if radii from the ring generated

by the wall with no liquid on it are subtracted from the radii of the ring created with liquid present, the height of the film can be calculated. A video camera is used to record the ring movement from which individual frames are selected and analyzed to determine the reflected light ring radii. Film heights are then calculated manually. The technique is verified to within 1% of static measurements made by the needle-contact method over a film thickness range of 0.5 mm to 12 mm. Film height data are presented from horizontal, annular, two-phase air-water flow with values ranging from 0.15 mm to 1.40 mm. Precision of 0.01 mm is attained with an estimated error of less than 10%. On the other hand, as presented, the technique is prone to slope errors of up to 20% and is quite time consuming to execute. Human judgement is required to determine the distance between a light source and the light pattern formed by the reflections at the liquid surface.

In spite of these difficulties, this technique is attractive because it is not limited to any particular position on a test section. All that is required is a transparent test section. Data may be taken at any location along or around the flow, allowing for detailed measurements of the liquid film as the flow develops and evolves. In addition, the technique is not limited to water, but may be used with any fluid which does not heavily absorb the light generated by the light source.

The purpose of this investigation is to significantly enhance the optical technique developed by Hurlburt and Newell. An automated system has been developed to obtain film height measurements which significantly reduces the measurement error of the original implementation. In addition, human judgement and error is essentially eliminated, and the amount of data that can be acquired is increased by the use of a computer-based video image processing system. The result is a simple, low-cost, flexible and accurate measurement system for the determination of the distribution of a liquid film on a surface.

# Chapter 3

# Theory of measurement by total internal reflection

## 3.1 Total Internal Reflection

The method developed in this work, based on the work of Hurlburt and Newell, relies on the principle of total internal reflection of light rays. As shown in Figure 3.1, a light ray traveling through one medium into another will be bent due to the fact that the speed of light is different among the two media. Light travels faster as density decreases, and the ray bends toward the interface to accommodate this change. This is described by Snell's Law:

$$n_1 \sin\theta_1 = n_2 \sin\theta_2, \tag{3.1}$$

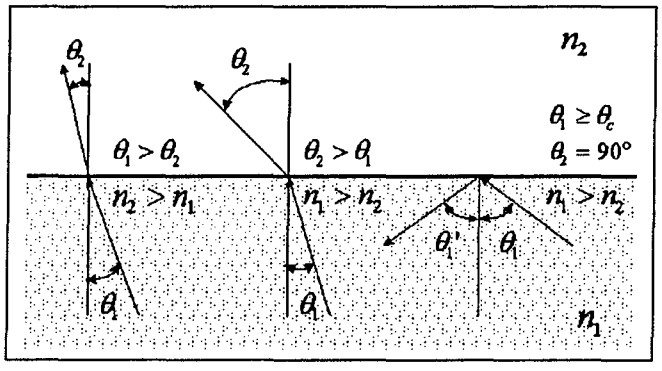


Figure 3.1: Relationships between light ray angles and the indices of refraction of two different media.

where $n_1$ and $n_2$ are the indices of refraction of the two mediums and $\theta_1$ and $\theta_2$ are the angles between the rays and the normal to the interface at the point the where the rays intersect the interface. As evident in Figure 3.1, when $n_2 > n_1$, a light ray entering medium 2 will be bent toward the normal, or away from the surface. As $\theta_1$ increases, $\theta_2$ increases as well, but not as rapidly. When $n_1 > n_2$, however, the ray will enter medium 2 bent toward the interface between medium 1 and medium 2. Now, $\theta_2$ will increase rapidly with increasing $\theta_1$ until $\theta_2 = 90°$. At this point, none of the light will be transmitted through the interface into medium 2. The situation diagramed in the far right of Figure 3.1 indicates that this occurs when $\theta_1 = \theta_c$, the critical angle for the two materials. Formally, this can be calculated from Snell's Law, Equation (3.1), with $\theta_2 = 90°$ and $\theta_1 = \theta_c$,

$$\sin\theta_c = \frac{n_2}{n_1}. \tag{3.2}$$

Any ray arriving at the interface with an angle greater than or equal to the critical angle, $\theta_c$, will be completely reflected back into the first medium.

Although ignored in the above discussion, some fraction of the first, usually called incident, ray is always reflected from the surface back into the original medium. This can be seen in Figure 3.2. The amount of light reflected (or transmitted) can be determined from Fresnel's relations, given here as

$$r_{TE} = \frac{\cos\theta - \sqrt{n^2 - \sin^2\theta}}{\cos\theta - \sqrt{n^2 - \sin^2\theta}} \tag{3.3}$$

for the transverse electric mode of propagation, and

$$r_{TM} = \frac{n^2\cos\theta - \sqrt{n^2 - \sin^2\theta}}{n^2\cos\theta - \sqrt{n^2 - \sin^2\theta}} \tag{3.4}$$

for the transverse magnetic mode, where $n = n_2/n_1$ is the ratio of the two indices of refraction and $\theta$ is the angle between the incident light and the normal of the interface. If random polarization is assumed, the average reflectance, which is defined as the percentage of the incident light that is reflected at the interface, may be calculated by averaging the squares of the polar reflection coefficients defined by Fresnel's equations: $R_{avg} = \frac{r_{TE}^2 + r_{TM}^2}{2}$ [1]. The average

[1]The Fresnel equations actually generate values for the ratio of the outgoing electric field

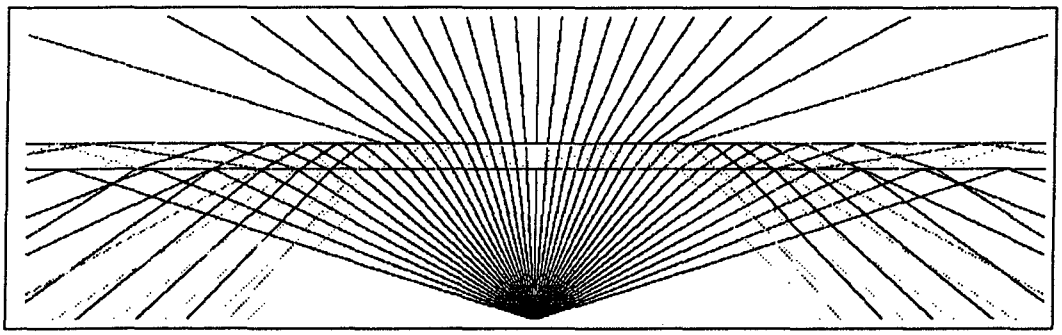

Figure 3.2: Simulation of total internal reflection when light rays travel through glass (n =1.5) into water (n=1.33).

transmittance, or percentage of light intensity transmitted through the interface, is then $T_{avg} = 1 - R_{avg}$.

If the ratio of the two indices of refraction is less than one ($n_2 < n_1$), a ray leaving the source can arrive at the surface with an angle greater than or equal to the critical angle, and the transmitted ray will be bent so that it is parallel with the surface. The critial angle determined by Equation (3.2) can also be determined from the Fresnel equations as the angle which causes $\sqrt{n^2 - \sin^2\theta}$ to become complex. At this point the magnitude of the reflectivity becomes one, so the magnitude of the transmissivity of the light ray must become zero. Thus, all of the energy in the incident light ray is reflected from the interface. This condition is called total internal reflection. The fact that the reflectivity is now complex indicates that a phase shift must occur at the reflection.[2]

## 3.2 Determining Film Height

Figure 3.2 displays the simulated results of rays leaving a point source diffusely and interacting with a wall medium (n = 1.5), liquid (water, n = 1.33) and air (n = 1.00). The first ray to be reflected completely must have reached the

intensity to the incoming electric field intensity (TM or TE), $r = E_o/E_i$. Reflectance is the ratio of the outgoing to incoming *powers*: $R = P_o/P_i$. Since the electric field power is directly proportional to the intensity squared ($P \propto E^2$), the reflectance may be calculated as the ratio of the outgoing to incoming field intensities squared, which is equivalent to squaring the reflection coefficients of Equations (3.3) and (3.4): $R = E_o^2/E_i^2 = r_{TE}^2$ (or $r_{TM}^2$). (See, for example, Pedrotti and Pedrotti; 1993, pp. 407 - 414)

[2]For the purposes of this method, light rays of random phase are assumed, so this phase shift will be ignored.

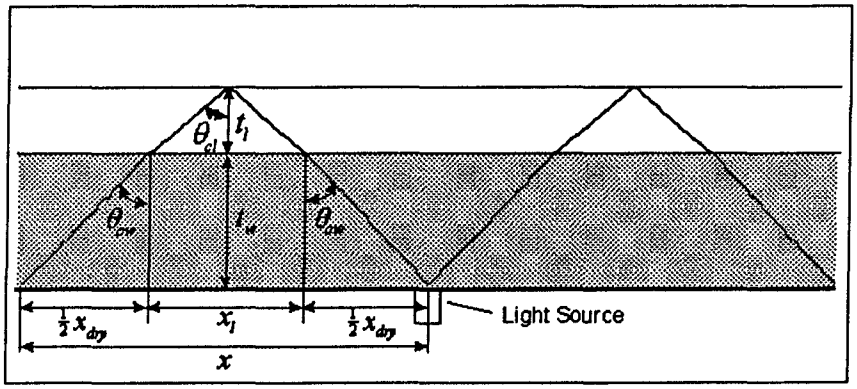


Figure 3.3: Calculating liquid film thickness

water/air interface at the critical angle. With this knowledge, the dimensions of the system can be completely determined from the optical properties of the wall, liquid and gas. This is the basis of the film thickness measurement system.

The first step, then, is to relate the distance between the light source and the reflected rays to the thickness of the liquid film. Figure 3.3 shows the geometrical relationships defined by the liquid and wall dimensions, $t_l$ and $t_w$, the critical angles, $\theta_{cl}$ and $\theta_{cw}$, and the linear distances along the outer test section wall. From this diagram, $x_l$, the linear distance traveled by the light ray as it moves through the liquid, is given by

$$x_l = 2t_l \tan\theta_{cl},$$

where $\theta_{cl}$ is the critical angle between the liquid and the vapor (which can be assumed to behave optically as air). Thus,

$$t_l = \frac{x_l}{2\tan\theta_{cl}}. \tag{3.5}$$

Next, the total distance between the light source and the reflection point on the outer wall, $x$, is

$$x = \frac{1}{2}x_{dry} + x_l + \frac{1}{2}x_{dry},$$

or

$$x = x_l + x_{dry}.$$

But

$$\frac{1}{2}x_{dry} = t_w \tan\theta_{cw},$$

where $\theta_{cw}$ is the critical angle of the wall–*air* interface. (Note that this is *not* the critical angle of the wall–liquid interface. See Appendix A for a detailed explanation of this.) So,

$$x = x_l + t_w \tan\theta_{cw},$$

and

$$x_l = x - t_w \tan\theta_{cw}.$$

Substituting this into (3.5),

$$t_l = \frac{x - t_w \tan\theta_{cw}}{2\tan\theta_{cl}}. \tag{3.6}$$

Since $t_w \tan\theta_{cw}$ is a constant equal to $x_{dry}$ for a given wall material and thickness, it is sometimes useful to write Equation (3.6) as

$$t_l = \frac{x - x_{dry}}{2\tan\theta_{cl}}.$$

Equation (3.6) now relates the film thickness, $t_l$, with the distance, $x$, between the reflected light ray at the outer test section wall and the light source. If (3.6) is written as

$$t_l = \frac{x}{2\tan\theta_{cl}} - \frac{x_{dry}}{2\tan\theta_{cl}},$$

it is readily apparent that the relationship between the film thickness and the distance traveled by the light ray is linear. This is further demonstrated by Figures 3.4 and 3.5. Figure 3.4 demonstrates that $x_{dry}$ remains constant while $x_l$ varies linearly with $t_l$. In Figure 3.5, it can be seen that $x_l$ remains constant for a given $t_l$ even though the wall thicknesses are quite different.

## 3.3 Determining the Height of a Film with a Sloping Surface

The geometries of flowing films can be quite complex. Using flow visualization techniques and the film measurement techniques described in Chapter 2, many investigators have uncovered some detail of the flow conditions (Sattelmayer et al.; 1987; Hewitt et al.; 1990; Jayanti et al.; 1990; Paras and Karabelas; 1991). While most flows contain significant amounts of roughness in the form

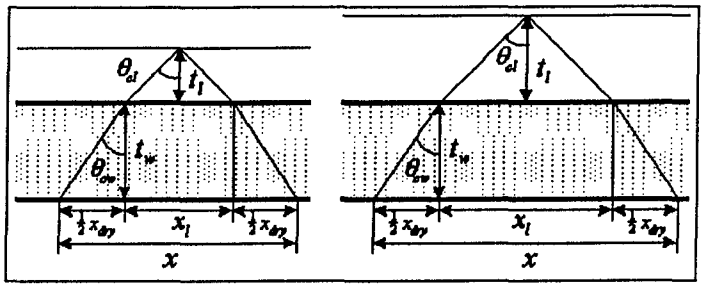


Figure 3.4: Demonstration of linear variation of $x_l$ with $t_l$. $x_l$ varies linearly with $t_l$ while $x_{dry}$ remains constant.

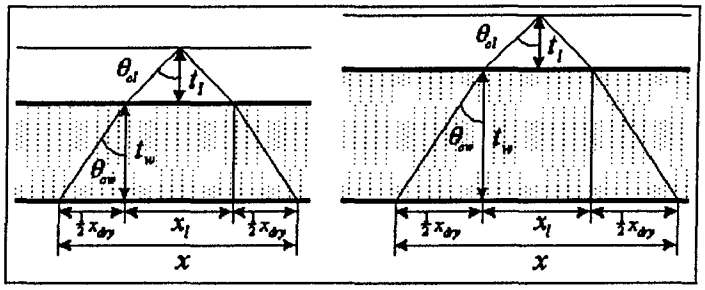


Figure 3.5: The effect of changing wall thickness. $x_l$ remains constant for a given $t_l$ even though $t_w$ changes significantly.

of small to moderate waves and entrained bubbles of various sizes, it is observed that as the liquid film becomes quite thin ( less than 0.5 mm, say), the surface smooths considerably. In addition, the effects of surface tension and viscosity will tend to dampen the surface structure in many fluids.

Assuming, then, that the fluid surface is on average smooth enough to reflect the light back, the effect of long-wavelength (much greater than the diameter of the test section) structures needs to be considered. An analysis of the error resulting from assuming that no slope exists on the liquid surface indicates that even a slope as small as 5 degrees can lead to errors of several hundred percent. [3] It is important, then, that this situation be understood so that appropriate compensation can be made. [4]

The relationships for the sloping interface can be derived with reference to Figure 3.6.

$$x_l = t_l \tan(\theta_{cl} + \phi) + t_l \tan(\theta_{cl} - \phi), \tag{3.7}$$

where $x_l$ is the linear distance traversed by the light ray as it travels through the liquid, $t_l$ is the height of the liquid at the reflection point, $\theta_{cl}$ is the critical angle of the liquid-vapor interface, and $\phi$ is the angle the sloping liquid surface makes with the horizontal. Substituting the trigonometric identities,

$$\tan(\alpha + \beta) = \frac{\tan\alpha + \tan\beta}{1 - \tan\alpha\tan\beta}$$

and

$$\tan(\alpha - \beta) = \frac{\tan\alpha - \tan\beta}{1 + \tan\alpha\tan\beta}$$

into (3.7) gives

$$x_l = t_l \left( \frac{\tan\theta_{cl} + \tan\phi}{1 - \tan\theta_{cl}\tan\phi} + \frac{\tan\theta_{cl} - \tan\phi}{1 + \tan\theta_{cl}\tan\phi} \right).$$

Simplifying and solving for $t_l$,

$$t_l = \frac{x_l}{2\tan(\theta_{cl})} \left( \frac{1 - \tan^2(\theta_{cl})\tan^2(\phi)}{1 + \tan^2(\phi)} \right) \tag{3.8}$$

[3] This can be verified by performing a few sample calculations of film thickness using Equation (3.6) and comparing with the expression to be determined next for the sloping surface, Equation (3.8).

[4] For the purposes of this discussion, the surface is assumed to slope only in one plane and hence the problem can be analyzed using 2-D models. This assumption does not significantly limit the accuracy of the measurement system described later. Because a narrow width of the reflection image is sampled, if rays are reflected transversely by a 3-D wave, the rays will, in general, still be sampled and averaged together.

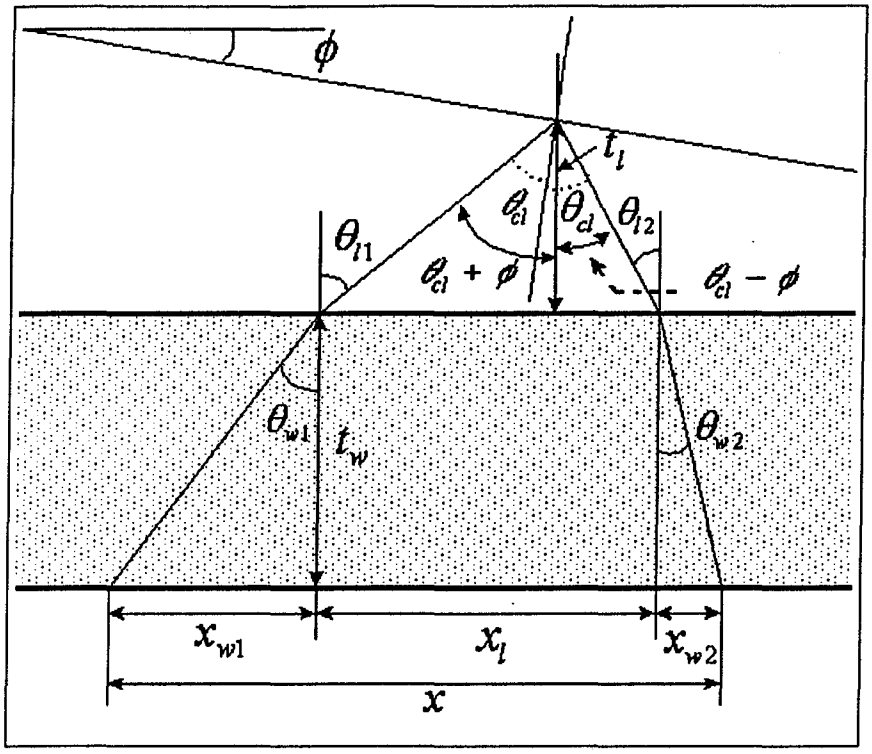


Figure 3.6: Geometries of light rays with a sloping liquid surface.

Next, a relation between $t_l$ and the total linear distance traversed by the light between the source and the reflection, $x$, must be obtained. From Figure 3.6,

$$x_l = x - (x_{w1} + x_{w2}), \tag{3.9}$$

where $x_{w1}$ and $x_{w2}$ are the linear distances traversed by the light as it travels through the wall given by

$$\begin{aligned} x_{w1} &= t_w \tan\theta_{w1} \\ x_{w2} &= t_w \tan\theta_{w2}. \end{aligned} \tag{3.10}$$

$\theta_{w1}$ and $\theta_{w2}$ are the angles made by the light ray with the wall surface normal at the wall-liquid interface. Recall that these angles were both equal to $\theta_{cw}$ when the surface of the liquid was assumed parallel with the wall surface. A relation between these angles, the liquid surface slope, $\phi$, and the liquid-air critical angle, $\theta_{cl}$, can be determined from Snell's Law. Beginning with $\theta_{w1}$ and referring again to Figure 3.6,

$$n_l \sin\theta_{l1} = n_w \sin\theta_{w1}.$$

Due to the fact that the opposite interior angles of two parallel lines are equal,

$$\theta_{l1} = \theta_{cl} + \phi,$$

and

$$n_l \sin(\theta_{cl} + \phi) = n_w \sin\theta_{w1}.$$

Expanding $\sin(\theta_{cl} + \phi)$,

$$n_l(\sin\theta_{cl}\cos\phi + \cos\theta_{cl}\sin\phi) = n_w \sin\theta_{w1}.$$

But, since

$$\theta_{cl} = \sin^{-1}(1/n_l),$$

$$\sin\theta_{cl} = 1/n_l.$$

Substituting and solving for $\theta_{w1}$,

$$\theta_{w1} = \sin^{-1}\left(\frac{\cos(\phi) + n_l\cos(\theta_{cl})\sin(\phi)}{n_w}\right). \tag{3.11}$$

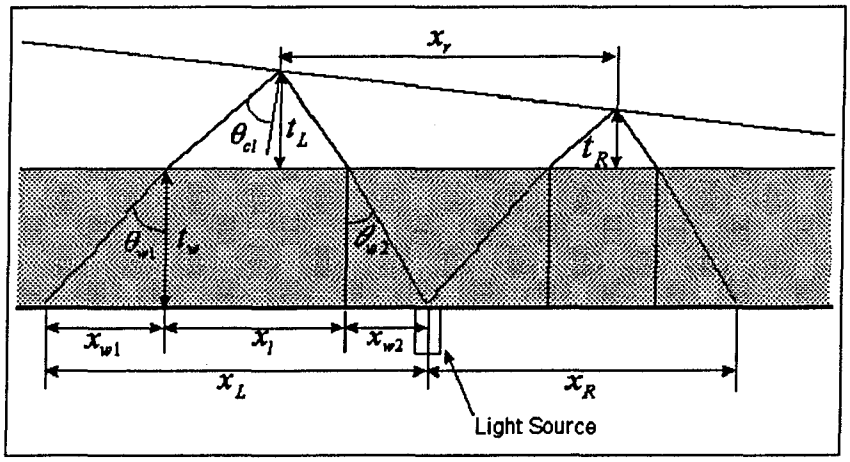


Figure 3.7: Calculating surface slope and film thicknesses: One light source.

A similar operation produces

$$\theta_{w2} = \sin^{-1}\left(\frac{\cos(\phi) - n_l\cos(\theta_{cl})\sin(\phi)}{n_w}\right). \tag{3.12}$$

Now, Equations (3.8) – (3.12) completely determine the geometry of the light ray reflected from a sloping surface provided the distance between the light source and the reflected ray ($x$) can be measured and a relationship between the slope of the surface and the film heights is known. To provide this additional relation, an additional reflection point is required. Figures 3.7 and 3.8 show how two reflection points are obtained from one light source and two light sources, respectively.

Using the dimensions defined in Figures 3.7 and 3.8, the slope of the surface ($\phi$) is determined by,

$$\phi = \tan^{-1}\left(\frac{t_L - t_R}{x_r}\right) \tag{3.13}$$

where $t_L$ and $t_R$ are the heights of the liquid at the two reflection points, and $x_r$ is the horizontal distance between the two reflection points.

The calculation of $x_r$ depends on whether the single source or dual source configuration is used. From the geometry of Figure 3.7,

$$x_r = t_w(\tan\theta_{w1} + \tan\theta_{w2}) + t_L\tan(\theta_{cl} - \phi) + t_R\tan(\theta_{cl} + \phi). \tag{3.14}$$

The two source configuration in Figure 3.8 gives

$$x_r = d_{src} - \{t_w(\tan\theta_{w1} + \tan\theta_{w2}) + t_L\tan(\theta_{cl} + \phi) + t_R\tan(\theta_{cl} - \phi)\}. \tag{3.15}$$

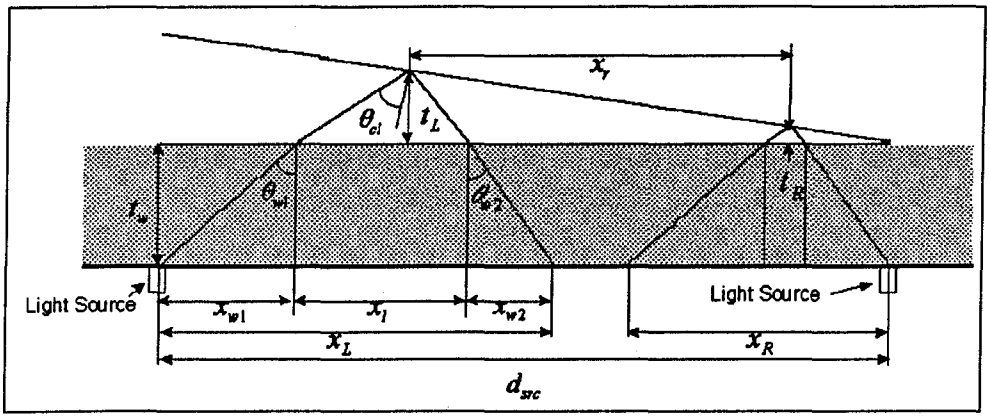


Figure 3.8: Calculating surface slope and film thicknesses: Two light sources

Using a single source has the advantage of simplicity of positioning, more localized measurement and not needing to determine $d_{src}$, a measurement that may be difficult to do with precision. On the other hand, because the technique uses images of the reflected light obtained by a camera beneath the light source(s), mounting a single source in the center of the camera's field of view will block a part of the image that could otherwise be used for measurement. In addition, the position of the source would slightly complicate the image processing algorithm.

For these reasons, the measurement system has been implemented using the two source configuration, and this will be assumed in the remaining sections of this work.

## 3.4 Finding the First Fully Reflected Ray

Central to the calculation of the film height is the measurement of the distance between the light source and the first fully reflected ray, as this is the only ray which reflects from the liquid-vapor interface at the critical angle, an essentially constant value determined by physical properties of the materials. Figure 3.9 depicts a simulation of light rays originating from a point source and reflecting back from an air/water interface. The first fully reflected ray is quite easy to determine from this image. However, the path of one photon, or one ray of light, or even several photons, can not be isolated from a large number precisely by any detector. All photon detectors, including human eyes, CCD

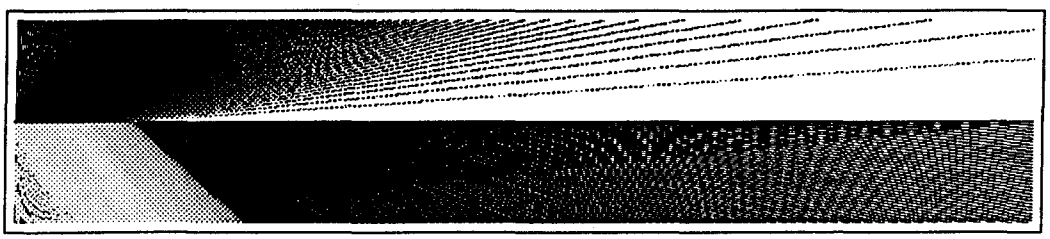

Figure 3.9: Simulation of light from a point source interacting with a glass-water interface. For better reproduction and clarity, the "light" rays are actually dark in this image; the darkest rays have the most light power while the lightest rays contain the least. The light source is in the lower left corner.

arrays, photodiodes, and photomultiplier tubes, average the light received over some finite area. The perceived intensity is a measure of the amount of light energy received in a finite area per unit time (irradiance is a more precise term for this).

To investigate how the position of the first fully reflected ray may be determined, a simulation of light generated by a point source and reflected from a glass-air interface is presented in Figure 3.9. In this image, "light" rays are plotted as dark lines; the varying shades of gray from light to dark indicate increasing levels of light power (energy per unit time, as, for example, the number of photons passing a given point in a second). Rays with small angles of incidence at the glass-air interface pass through with virtually no loss. (A very small amount, about 4%, is reflected from the surface even in these cases. These reflected rays appear white in the image which is why the region near the light source is nearly completely white.) As the light rays fan out, a rather rapid transition occurs between the rays which are mostly transmitted to those which are completely reflected.

The values of the light power (energy per unit time) in each simulated reflected light ray striking the bottom surface are plotted as circles (o) in Figure 3.10. This is essentially a plot of the reflected light power versus distance from the source. The irradiance, or the intensity perceived by a photodetector, can be approximated by averaging the light power data over a small area. Repeatedly applying a low-pass (smoothing) filter along the light power curve generates a simulated intensity, or perceived brightness, curve, plotted as a solid line in Figure 3.10.

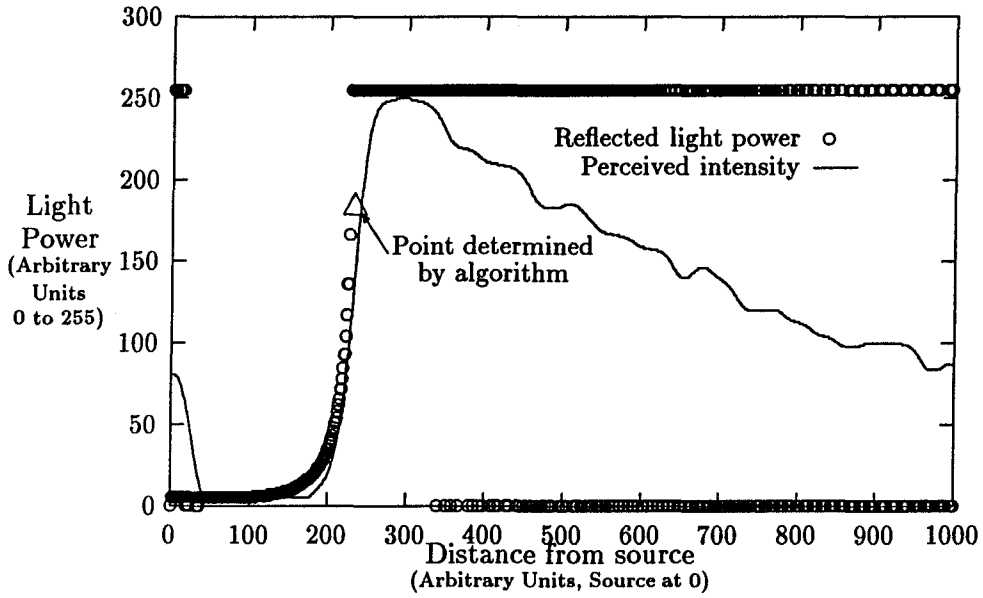


Figure 3.10: Locating the first fully reflected ray. The simulated light power reflected from the glass-water interface (the relative darkness of the rays striking the bottom of the image in Figure 3.9) is plotted with o's along with an approximation of the perceived brightness of the light on the outside of the wall and the point of steepest slope in the perceived brightness curve.

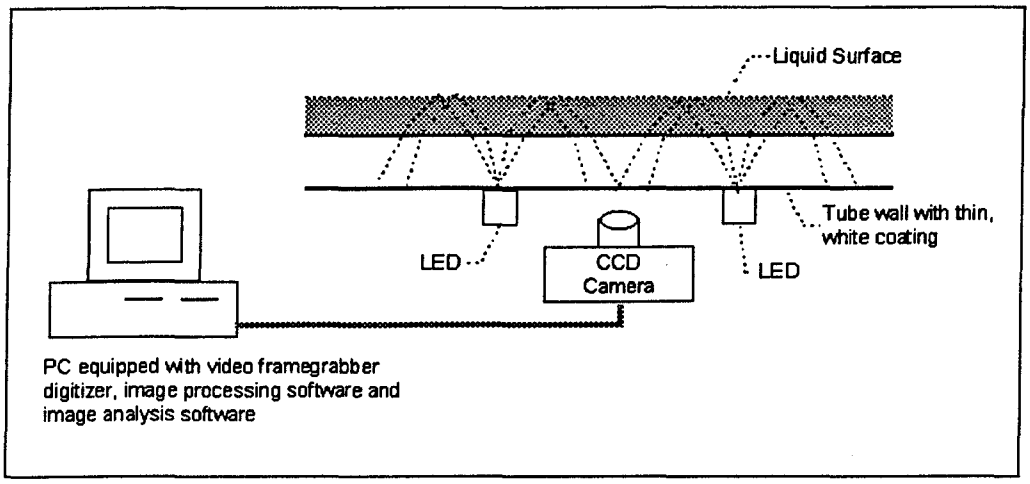


Figure 3.11: Schematic of the components of the film thickness system.

As can be seen in the figure, the point at which the first fully reflected ray returns to the outer surface is marked by a very steep rise in the intensities of the rays. If, then, the plot of light power were analyzed to determine the point of greatest slope, the location of the first fully reflected ray could be determined. This carries over to the plot of intensities, as well. The point of greatest slope in the intensity profile is marked by a triangle ($\triangle$), and it locates the first fully reflected ray to within 4 data points or about 0.4% in this simulation.

In addition, using this method reduces sensitivity to background light and fouling of the test section wall while removing any direct dependence on absolute light intensities, thus eliminating the need for frequent calibration.

## 3.5 The Experimental Setup

The experimental system must perform three primary functions: the generation of diffuse light rays, the capture of light reflected from the liquid surface, and the analysis of the reflected light rays to determine the height of the liquid. Figure 3.11 shows a schematic diagram of a possible measurement system.

Light is generated by two high-brightness light emitting diodes (LED's) which can be easily mounted on the outside of a test section. The diffusing lens of each LED (the rounded top) is removed down to a point very near

the light generating element. An opaque mask is painted onto the LED case so that the light output is restricted to a small area directly above the light element, preventing stray light from interfering with the measurement process.

A low-power laser may be used as the light source. Advantages include the ability to focus the beam very tightly, better approximating a point source, and higher brightness. It may also be possible to perform detailed analysis on polarizing and phase shifting phenomena which could provide a significant amount of information about the liquid surface. Care must be taken, however, to ensure the damage threshold of the test section material is above the focused power density of the beam. In addition, lasers containing significant energy in the blue wavelengths may deteriorate plastics rapidly, and other materials may be sensitive to particular common wavelengths (as Pyrex is to large power densities in the green wavelengths). Finally, delivering the beam to the test surface is not trivial, limiting mobility, and vibration of the test section, optics and laser head may significantly deteriorate any accuracy gained.

A thin, light, semi-opaque coating is applied to the outer wall of the test section. This homogenizes the light leaving the LED's and helps to distribute light diffusely. In this particular setup, thin, frosted, plastic tape with a white adhesive is used. Note that no air gaps can exist between the coating and the test section wall. Even a thin air layer will cause light rays traveling at an angle equal to or greater than the critical angle of the coating-air interface to be reflected away from the test section, leaving very little light to enter the test section wall at an angle such that it may arrive at the liquid-gas interface with an angle equal to or greater than liquid-gas critical angle.

White spray paint has been used successfully for the semi-opaque coating. The disadvantages of this are its graininess, permanence, and the difficulty in generating an even coating. As an alternative, white spray paint has been applied to a thin sheet of clear plastic, and this plastic sheet placed on the test section with a thin layer of water or oil between them to act as an optical coupling.

Since most, if not all, of the light reflected from the liquid-gas interface will arrive at the outer wall surface at an angle greater than the critical angle for the wall-air interface, without the coating, the light would reflect back into the wall and thus remain trapped there. The coating then serves to couple the

light out of the wall and then scatter it so that an image of the reflected light may be detected.

A video camera positioned near the test section can be used to capture this image for further analysis. In this implementation, a small, inexpensive, monochrome charge-coupled device (CCD) camera is mounted together with the LED's in a single unit which can be mounted at any location on the test section and easily moved, allowing for measurements to be taken both around and along the test section.

The video camera output may be recorded on standard video tape, played back, and frames selected to be measured. Whether the image analysis is performed manually or with an automated system, it is most convenient to use a video framegrabber peripheral to digitize the video signal and store the image on a computer. The image can then be manipulated and enhanced by one of the many image processing packages available.

Since using standard video recording technology can reduce image resolution nearly 60% (Russ; 1994), the implemented system grabs frames directly from the CCD camera for processing. The camera generates NTSC standard composite video with 512 vertical lines and 486 horizontal lines, though the limited bandwidth actually restricts the number of vertical lines to approximately 330 (Russ; 1994). The video framegrabber peripheral digitizes the signal, dividing the image into picture elements, or pixels. Each pixel is assigned a number, or numbers, specifying the brightness (if monochrome), or color and intensity (if color), that should be displayed at that location. This system uses a monochrome camera, so each pixel is assigned a value between 0, representing no light intensity, and 255, indicating maximum light intensity. The image is stored in computer memory as an array of pixels, 486 elements tall by 512 elements wide, occupying $512 \times 486 = 248{,}832$ bytes of memory.

Once stored in memory, the image can be analyzed and manipulated using discrete mathematical operations. By applying discrete filters, the gradient of the light intensities in the image can be generated, then the maximum gradient located and recorded. This value must then be converted to a physical distance, from which information about the liquid layer can be determined.

## 3.6 Image Processing Algorithm

As presented earlier, locating the first fully reflected light ray is achieved by determining the point of greatest slope in the light intensities generated by the reflected rays. The point of greatest slope in light intensities is found through several image processing steps. First, the image is split into two images, one composed of the even lines and one of the odd lines of the original image. The brightness contrast is then enhanced and a low pass filter is applied to the image to lessen random high frequency noise. A gradient filter is applied, and the pixels with the largest gradient value are then selected. Finally, a single pixel position is determined from these pixels as the point which will be designated the point of greatest slope.

Throughout the description of the processing which follows, it will be helpful to provide visual examples of each step. Figure 3.12 shows an actual image of a portion of the light reflected from the surface of a moving liquid. To demonstrate the image processing, the pixel intensity values for a single row, row 50, have been extracted and plotted below the original image. As each processing step is completed, a new intensity profile will be presented, clearly showing the effect of each processing step.

### 3.6.1 Odd and Even Images

NTSC standard composite video is interlaced. A single standard video image is composed of 486 horizontal lines of brightness and color which are completely redrawn every $30^{th}$ of a second. However, early television equipment was unable to generate consecutive lines with enough precision to generate a good image at this rate. Therefore, a standard was developed in which every other line is drawn first, then the remaining lines filled in. Thus, during the first $60^{th}$ of a second, the even lines (0, 2, ..., 486) are generated, while the odd lines (1, 3, ..., 485) are generated in the next $60^{th}$ of a second. This is what is referred to as interlacing, or interlaced video.

When a video camera is used to capture an image of the light reflected from the surface of a moving liquid film, essentially two images are obtained, each a $60^{th}$ of a second apart. If, for example, the film structure is moving at 0.5 m/s, it will travel 8 mm from the moment the even lines are imaged till the

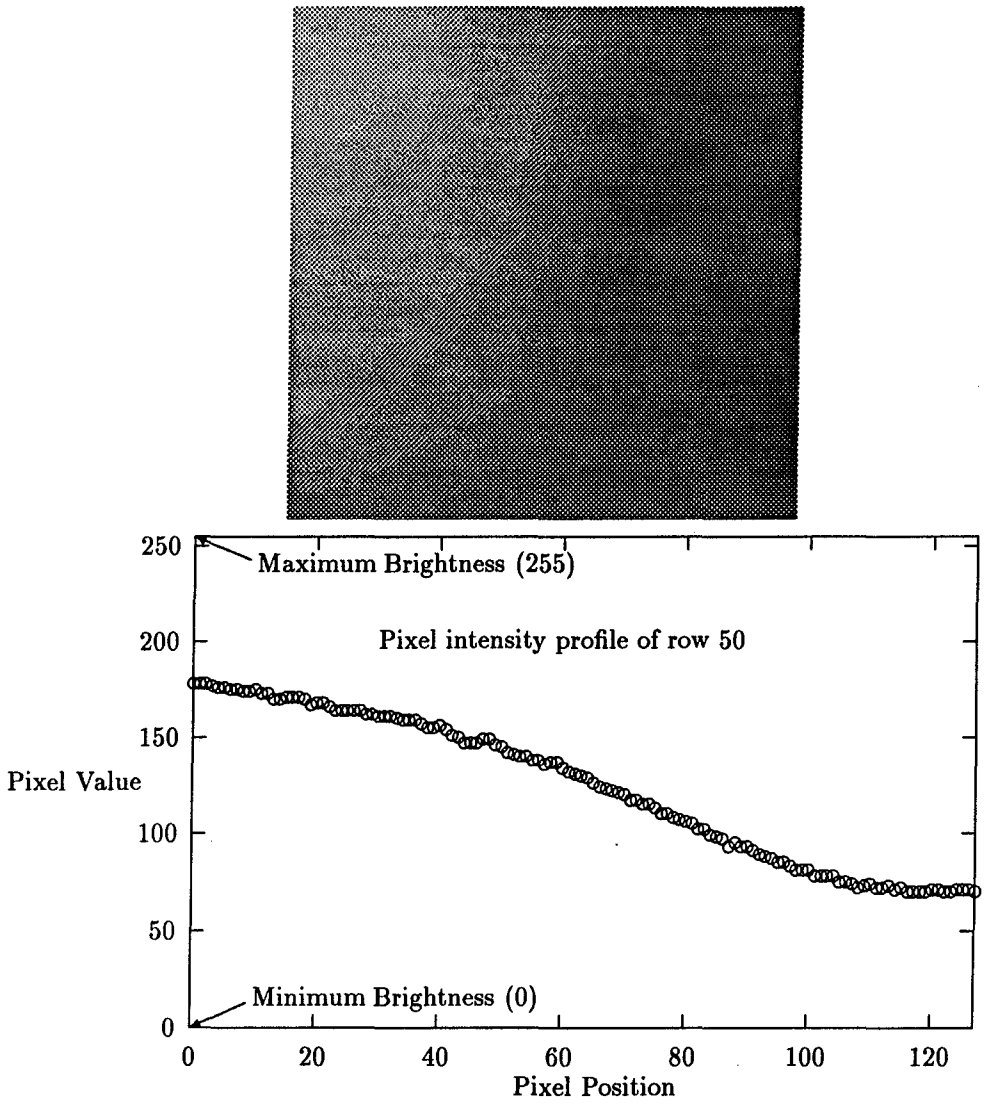


Figure 3.12: Processing one row of an image. The pixel intensities from row 50 of the top image have been extracted and plotted. This pixel intensity profile will be processed as an example of the processing performed to locate the position of the first fully reflected ray.

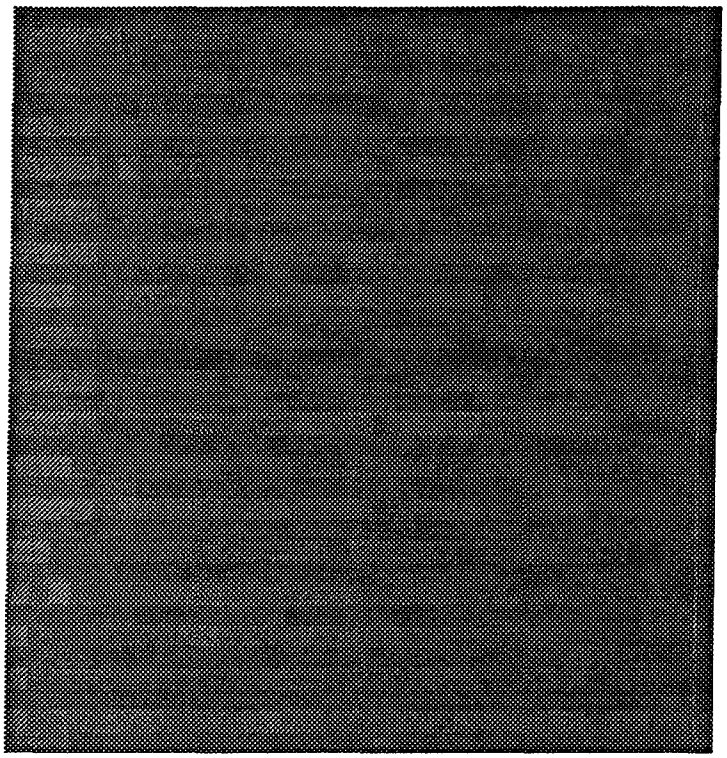

Figure 3.13: An interlaced image of moving liquid. This magnified view of an image of the light reflected from a moving liquid surface shows the difference in the odd and even images taken 1/60 s apart.

time the odd lines are imaged. In reality, liquid waves appear to be moving at speeds greater than 2 or 3 m/s. Thus, one image contains even and odd lines representing entirely different states of the liquid. This can be clearly seen in Figure 3.13. Fortunately, due to the way a CCD camera is implemented, all the lines of one field, odd or even, are imaged at the same instant, rather than over the entire 1/60 s interval.

The first step in determining the height of the liquid film, then, is to split the captured frame of video into its even and odd fields. This is a a straightforward operation, and provides the added benefit of giving an extra data point for each frame-grabbing operation. Figure 3.14 shows the results of this operation on the image in Figure 3.13.

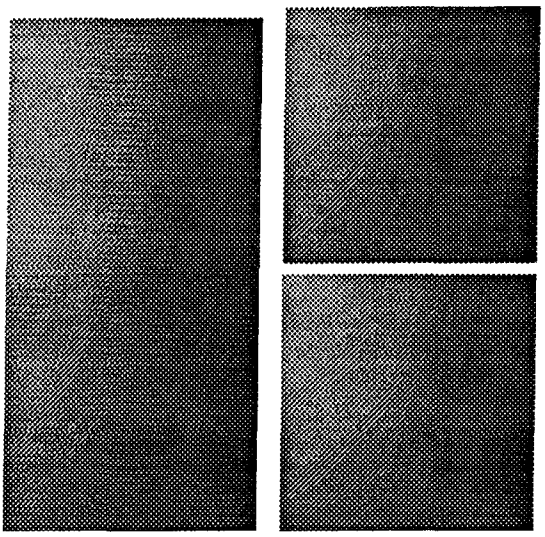

Figure 3.14: Splitting an interlaced image into odd and even images. The image on the left is an interlaced image which is split into its odd (top) and even (bottom) frames on the right.

### 3.6.2 Brightness Contrast Enhancement

Image contrast can essentially be defined as the difference between the brightest and darkest parts of an image. The greatest contrast a standard monochrome video image may have when digitized (using 8 memory bits per pixel) is 255, which indicates that the image has at least one pixel with an intensity of 255 (white) and at least one pixel with an intensity of 0 (black). Most images have much lower contrast; perhaps maintaining a difference in intensity between the brightest and darkest pixels of less than 100. (The contrast of the image in Figure 3.12 of about 100 as indicated by the intensity curve plotted below the image.)

The core of the image processing algorithm is in finding the peak gradient in the light intensity. This operation is in itself relatively insensitive to background light and should give the same maximum gradient whether the image has low contrast or high contrast. However, with a low-contrast image, the signal-to-noise ratio (SNR) may be very poor, making it difficult to filter the high frequency noise from the primary intensity signal. By applying a linear contrast enhancement to the image, the noise can be filtered significantly while still maintaining a high contrast image, decreasing the susceptibility of

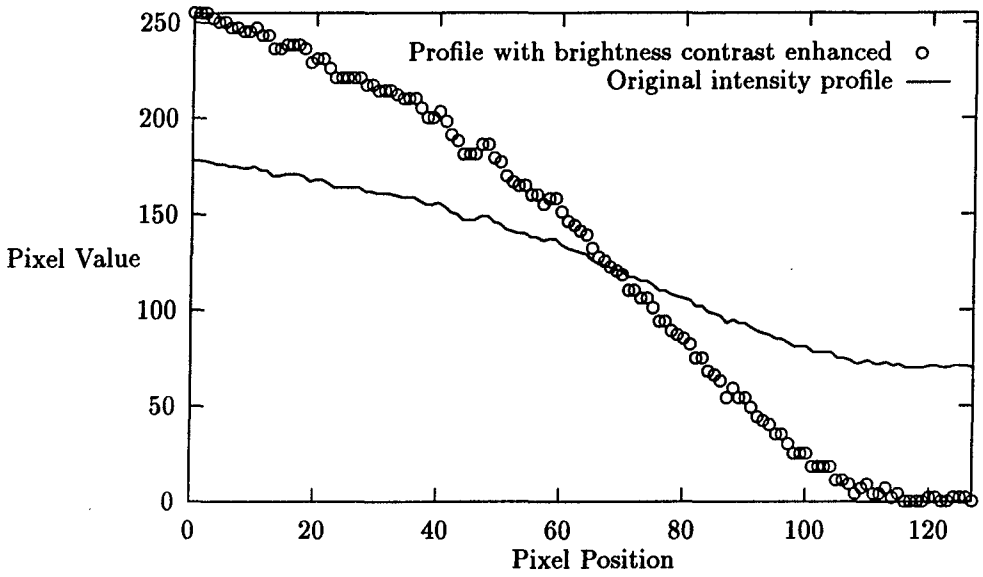


Figure 3.15: Brightness profile of contrast-enhanced pixel data.

the algorithm to random noise.

The linear contrast enhancement operation requires two steps. First, the entire image is scanned for its maximum and minimum pixel intensities. Next, each pixel is assigned a new intensity based on the linear relationship (Crane; 1997, p 55),

$$\text{new} = 255\left(\frac{\text{current} - \text{minimum}}{\text{maximum} - \text{minimum}}\right). \tag{3.16}$$

In effect, this takes the pixel with the minimum intensity value and gives it a new value of 0, while giving the maximum pixel a value of 255. Then, every other pixel is assigned a new value between 0 and 255 such that the new value will fit on the line defined by Equation (3.16). The result of performing a linear contrast stretch on the extracted brightness data from Figure 3.12 is shown in Figure 3.15.

### 3.6.3 Applying Filters to Image Data

The next two process steps involve a discrete convolution of the image data with a small set of fixed values. This is often referred to as applying a filter

to the image. Formally, the operation looks like this:

$$P(x,y) = \sum_{i=-n/2}^{n/2} \sum_{j=-m/2}^{m/2} I(i,j)F(x-i,y-j), \tag{3.17}$$

where $F$ is a filter composed of an array of values $n$ wide and $m$ tall, and $I$ is an $n \times m$ section of the image centered at $(x,y)$ (Gonzalez and Woods; 1992, p 108).

To implement this, the value of the pixel at $(x,y)$, $P(x,y)$, is simply the sum of the products of $I(i,j)$ and $F(i,j)$. Often, the final value is multiplied by some fixed constant, or a constant is added, to give a resulting pixel value between 0 and 255. Examples will be given in the following sections which should help make this operation more clear.

Further simplifications and reductions in the number of computations can be made if the filter can be written as $F(i,j) = g(i)h(j)$. Due to the linearity of the convolution sum, the convolution can be performed as two one dimensional sums versus one two-dimensional sum (Gonzalez and Woods; 1992, pp 128–130). For a $3 \times 3$ filter, 9 multiplications and 9 additions must be performed for each pixel in an image. If this filter can be split into two $1 \times 3$ filters, only 6 multiplications and 6 additions are required. This saves nearly 196,000 operations on a relatively small, $256 \times 256$ pixel image.

### 3.6.4 Low-Pass Filtering

Small variations in the pixel values of the image of the reflected light are not significant to the measurement. On the contrary, these variations are magnified many times by the gradient operation, causing difficulties in determining the slope of the overall light intensity curve. Hence, before a gradient is performed, a low-pass filter is applied to the image.

The filtering is achieved by an averaging operation. Each pixel is given the value of the average of all the pixels in a neighborhood around it. A two dimensional filter, or mask, to perform this task might be:

$$\begin{Bmatrix} 0.111 & 0.111 & 0.111 \\ 0.111 & 0.111 & 0.111 \\ 0.111 & 0.111 & 0.111 \end{Bmatrix}.$$

When this mask is convolved with the image data, a new pixel value is generated equal to $1/9 \sum$(the original pixel + surrounding pixels). For example, if the above mask is applied to the following data,

$$\begin{Bmatrix} 5 & 7 & 6 \\ 6 & 9 & 3 \\ 3 & 7 & 4 \end{Bmatrix},$$

the new pixel value for the center pixel (currently a 9) will be (0.556 + 0.778 + 0.667 + 0.667 + 1.00 + 0.333 + 0.333 + 0.778 + 0.444) = 5.56 $\overset{round}{\rightarrow}$ 6. (Pixel values must be positive integers to make sense.)

Note, however, that this same result can be achieved by using two $1 \times 3$ filters, one applied vertically and one applied horizontally: $\begin{Bmatrix} 1 \\ 1 \\ 1 \end{Bmatrix}$ and {0.111 0.111 0.111}. Application of the vertical filter to the above data will give {14 23 13}. Following with the horizontal filter gives {1.556 + 2.556 + 1.444}, or $5.56 \rightarrow 6$.

Because of the degree of smoothing required in this application, a filter of at least 11 terms is necessary. Rather than using an $11 \times 11$ array, two $1 \times 11$ filters are used, saving 198 operations per pixel. The result of performing the smoothing operation on the contrast-enhanced data in Figure 3.15 is shown in Figure 3.16

For further information on how this averaging process acts as a low-pass filter, see Appendix B.

### 3.6.5 The Gradient

Once the image data is smoothed, the gradient operator is applied. The convolution method is used as it was with the low-pass filter, but with

{0 0 0 0 0 1 -1 0 0 0 0 0}

as a mask. This detects increasing light intensity from right to left in the image: if the current pixel (at the -1 position in the mask) has a lower value than its left neighbor, the sum of the two ($-1 \times$ {current pixel} $+ 1 \times$ {left neighbor}) will be positive indicating an increase in light intensity from right to left. Decreasing light intensity will result in a negative value and a value of zero is assigned to

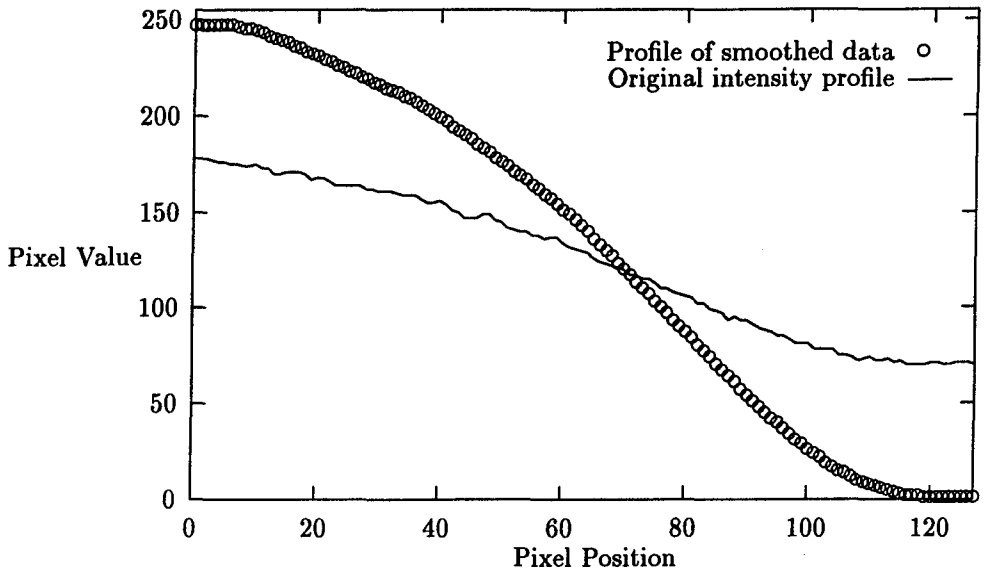


Figure 3.16: Brightness profile of smoothed pixel data.

that pixel. The leading and trailing zeroes are necessary to compensate for the size of the averaging mask. No horizontal smoothing occurs in the five pixels at left and right edges of the image, therefore, any gradient value determined within those regions will be erroneous and may be very large.

Similarly, using

$$\{0\ 0\ 0\ 0\ 0\ -1\ 1\ 0\ 0\ 0\ 0\ 0\}$$

as a mask will indicate increasing light intensity from left to right in the image.

Figure 3.17 shows the results of applying the gradient to the data in Figure 3.16.

## 3.7 Locating the point of Maximum Gradient

The next step is to isolate the maximum values in the image of gradient data. This is done one row at a time, in two steps. First, the row data is searched and the maximum value stored. Next, each pixel in the row is compared to this maximum value; if it is less, the pixel is given a value of zero, leaving only the pixels whose values are equal to the maximum value. An example of this is shown in Figure 3.18.

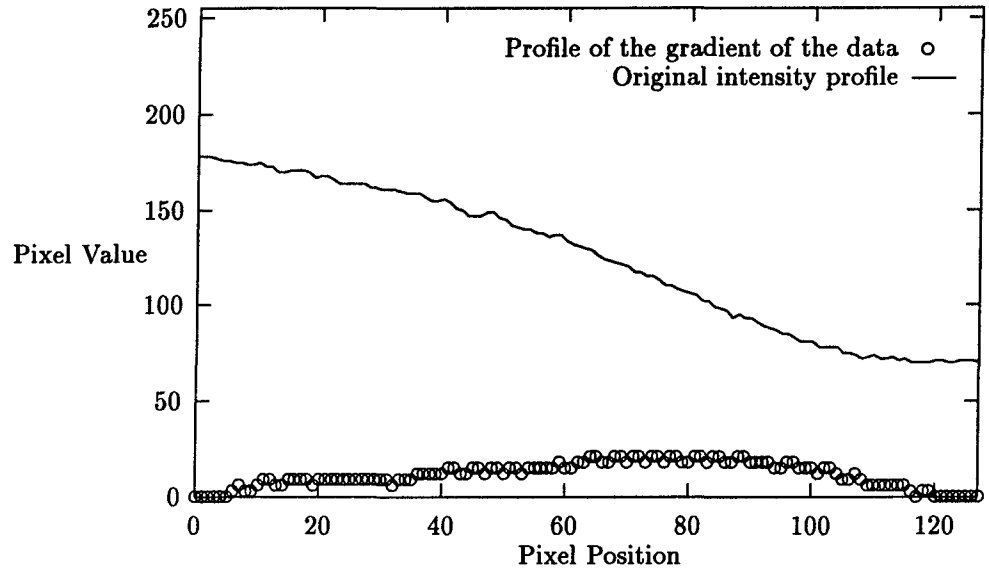


Figure 3.17: Brightness profile of the gradient applied to the data in Figure 3.16.

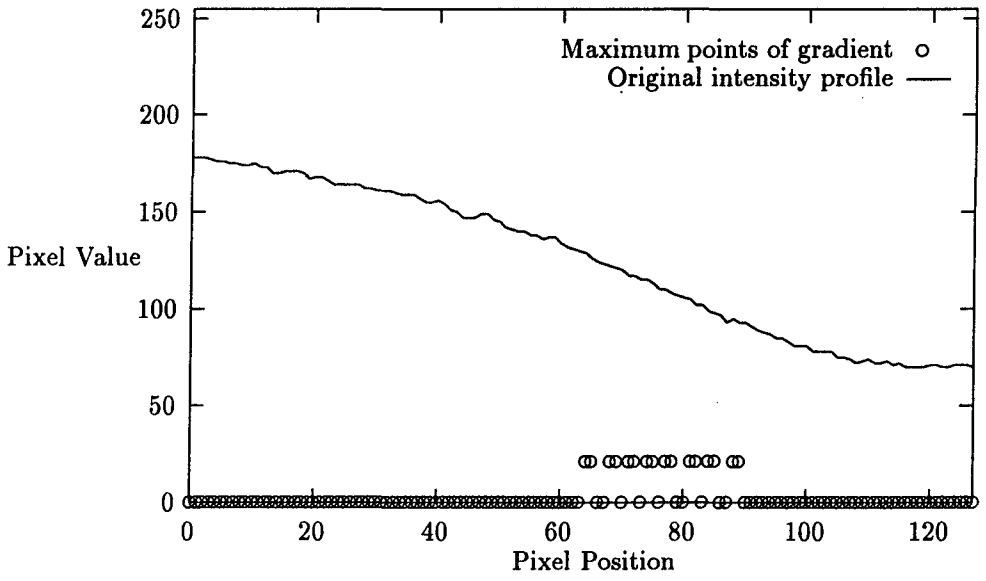


Figure 3.18: Maximum values of the gradient profile in Figure 3.17.

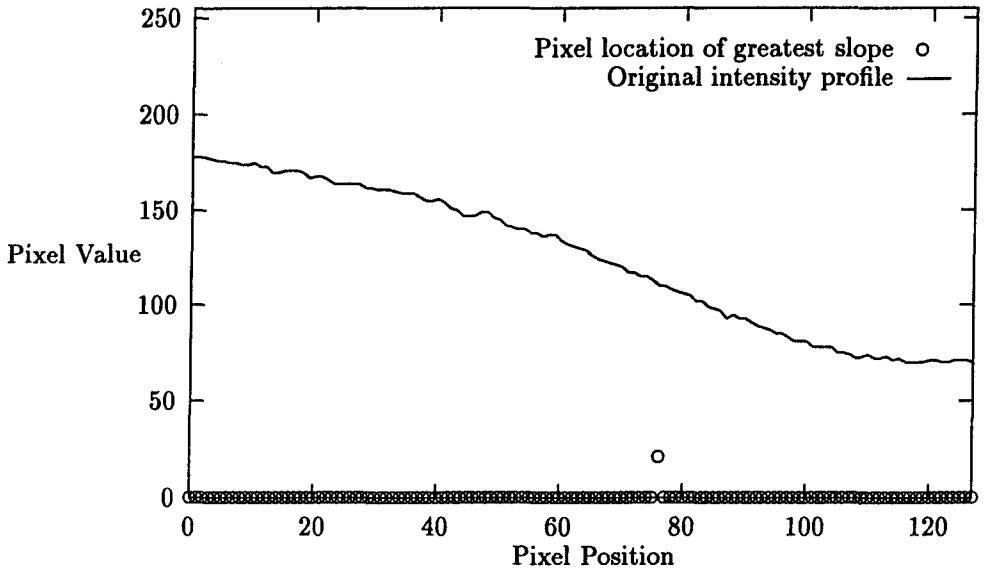


Figure 3.19: The single non-zero data point marks the pixel location of the greatest slope in the original brightness profile.

Since it is quite likely that some points of the light intensity curve are linear, it is possible that multiple pixels will have the maximum value, as is the case with the data in Figure 3.18. The assumption is then made that each of these pixels belong to the same region of maximum slope. A single point is selected by locating the edges of this region of maximum slope defined by the first and last pixels with values equal to the maximum value and giving all the pixels a value of zero except for the pixel at the center of the region. The result of this selection process for the data in Figure 3.18 is shown in Figure 3.19.

This process is repeated for every row of the image, resulting in a curve representing a section of the ring of first fully reflected light rays. Figure 3.20 shows the result of processing each row of the image that has been used as an example in this discussion.

## 3.8 Defining Physical Distances

A narrow region of the reflected light image is analyzed as described above to determine the distance between the light source and the first fully reflected

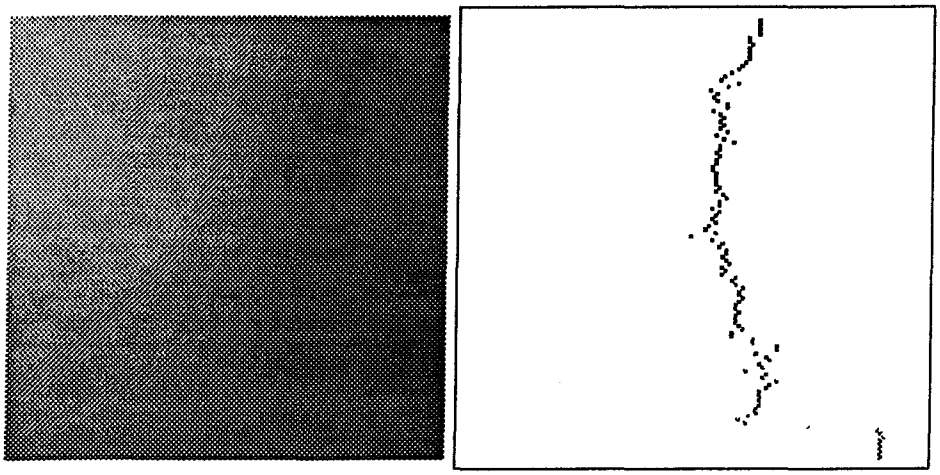

Figure 3.20: The image on the right is a result of processing each row of the image on the left as described in the text.

Figure 3.21: This image shows the processed surface reflection patterns from two light sources. The patterns represent points on the liquid surface separated by about 26 mm.

light rays. The narrow region is selected to be small enough such that curvature effects due to the circular light ring from the source and round test section wall distortions may be ignored. Yet the region should be large enough to average out random noise and small, unsteady, disturbances. The analyzed image will ideally result in a vertical line of pixels at some point in the image representing the location of the reflected light rays. However, the final reflection data may not generate a straight line due to vapor bubbles, the passage of a disturbance wave, or poor contrast in the image. Fouling or dust may cause minor distortions in the final image, as well. Figure 3.21 shows a typical processed image containing the reflection patterns from two light sources. The pattern on the left is relatively straight and its average pixel location can be used to estimate the distance between the light source and the fully reflected light rays. The pattern on the right, however, shows evidence of some significant flow disturbance; perhaps a sharp wavefront or bubble.

It is necessary, then, to use a robust mechanism for determining the horizontal location of the reflected light rays. To begin with, the mean horizontal pixel location, $\overline{x}$, is determined for the set of pixels and the standard deviation, $\sigma$, about this mean is calculated.

Next, a deviation term is calculated for each pixel based on its location with respect to the mean location:

$$\eta_{pix} = 1 - \frac{|x_{pix} - \overline{x}|}{4(1+\sigma)}. \tag{3.18}$$

If $\eta_{pix} < 0$, it is redefined to be equal to 0. This definition attempts to account for patterned and random variations in the individual pixel locations. First, if the pixel is far from the mean, the individual pixel should be considered an anomaly and not heavily weighted in final calculation of the reflected light position. The $4(1+\sigma)$ term in the denominator indicates that a pixel which lies greater than about 4 standard deviations from the mean will be completely ignored. Using $(1+\sigma)$ instead of $\sigma$ prevents a singularity when the pixel lies on the mean, and helps to prevent pixels near the mean from being eliminated from the averaging calculation when the standard deviation is less than 1.

The horizontal location that will be defined as the point at which the first fully reflected rays strike the outer wall, $x_{ref}$, is calculated by a weighted average of pixel locations:

$$x_{ref} = \frac{\sum \eta_{pix} x_{pix}}{\sum \eta_{pix}} \tag{3.19}$$

Finally, a confidence value is assigned to the calculated location. This takes into account the size of the standard deviation with respect to the total width of the image to help eliminate data that is badly scattered or bi-modal.

$$C = \frac{\sum \eta_{pix}}{N} \left( \frac{\text{image width} - \sigma^3}{\text{image width}} \right), \tag{3.20}$$

where $N$ is the number of different pixel locations averaged together. If $C < 0$, it is redefined to be equal to 0. The first term is the average of the individual pixel deviations, allowing the confidence value to account for the variation of the individual pixels. The $\sigma^3$ term causes the confidence to be strongly diminished by standard deviations greater than 1, causing scattered data to be removed from the final reported average.

At this point, the distance between the source and the reflected light, $x$ in Equation (3.9), can be calculated from

$$x = (x_{ref} - x_o)p_{scale} + x_{dry},$$

where $x_o$ is the location of the reflection of light from a dry wall surface, $p_{scale}$ is the pixel scale factor (mm/pixel) and $x_{dry}$ is the distance between the dry reflection point and the light source. $x_o$, $p_{scale}$, and $x_{dry}$ are determined by the calibration procedure described in Chapter 4.

After the pixel location is determined for the reflections from both light sources, the film thickness and film slope may be calculated. Equations (3.8) – (3.13) and (3.15) are numerically solved for the surface slope, $\phi$, film thicknesses, $t_L, t_R$, and distance between reflections, $x_r$, using the regula falsi method. This is an efficient step, requiring only 3 to 5 iterations. (See Scheid (1988) for more information about the regula falsi method.)

Due to the automated nature of the measurement, several film thickness readings may be taken quickly. The values determined for each measurement are written to a data file along with their respective confidence values. When the results of several measurements are averaged together, the confidence number is used as a weight, so the measurements from less scattered data will have more influence in the final result. This is calculated as

$$\text{Average} = \frac{\sum_i C_i D_i}{\sum_i C_i}, \tag{3.21}$$

where the $C_i$ are the confidence values corresponding to the measured data, $D_i$. $D_i$ may in fact be the average film thickness, $t_l$, one of the individual film thicknesses determined by each source, $t_L$ and $t_R$, or the slope, $\phi$.

# Chapter 4

# Calibration

In theory, the optical method presented requires no calibration as it is based entirely on the optical properties of the materials within the test section. However, in practice, several details about the actual measurement apparatus need to be known before actual distances can be calculated, and the indices of refraction of the wall and/or the liquid may not be known a priori. Hence, an automated calibration procedure has also been developed to determine the following parameters:

- Index of refraction of the test section wall material
- Index of refraction of the liquid
- Pixel scale factor (mm/pixel)
- Test section wall thickness (mm)
- Distance between each light source and its first reflected ray from a dry surface (mm)

As a result, the only information needed prior to obtaining film thickness data is the distance between the two light sources and one of the following:

- Index of refraction of the test section wall material
- Index of refraction of the liquid
- Test section wall thickness (mm)

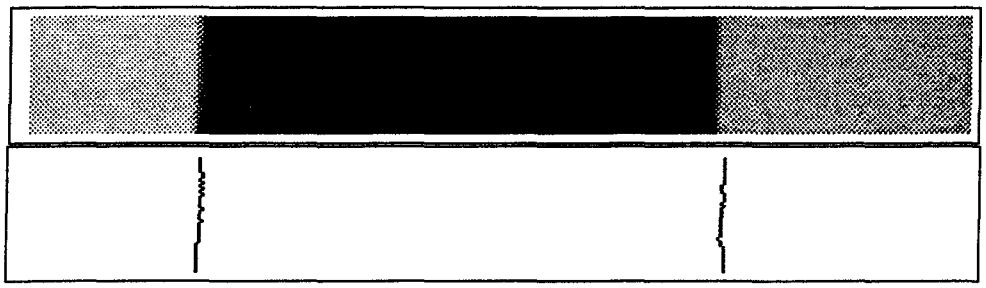

Figure 4.1: The top image is that of the piece of dark tape used to calibrate the pixel size of the video image. Below it is an image of the edges of the tape as determined by the image processing algorithm described previously. The tape is 12.55 mm wide and the pixel scale factor is 0.0707 mm/pixel.

## 4.1 Obtaining the Pixel Scale Factor

Among the most critical parameters needed is the pixel scale factor which relates a physical dimension to the pixel size. It is determined by the lens system of the camera, the size of the CCD array and the distance between the camera and the image. To obtain a value of the scale factor for a given set up, an object of known width is first placed in the center of the camera's field of view, such as the dark tape shown in Figure 4.1. Next, the image processing algorithm described above is used to locate the edges of the tape on the screen, as shown in the lower image of Figure 4.1. The distance between these edges is calculated in pixels, and the pixel scale factor is calculated using the actual physical width of the object provided by the operator. With the configuration used to obtain the images in Figure 4.1, the distance between the edges of the tape is 178 pixels. The tape is known to be 12.55 mm wide which gives a pixel scale factor of 0.0707 mm/pixel.

The pixel scale factor needs only to be determined once for a given camera/LED set up. The factor has been found to be very consistent, even after moving and re-mounting the camera apparatus several times.

## 4.2 Determining the Dry Wall Reference Values

From Figures 3.3 and 3.8, the distances between the light sources and the first fully reflected rays are the primary measured values needed to calculate the film thickness and slope. However, it is impossible to directly determine the position of the light sources in the image frame of reference, as the light sources are never themselves imaged. Therefore, some known reference position relative to each light source is needed. This is generated by locating the light reflected from the dry test section wall surface. The basic algorithm for obtaining this distance is:

- Obtain an image of the reflected light from both light sources with no liquid on the walls
- Process the image to find the pixel locations of the reflected light images of each source

Once these distances are known, the light sources can be located with the knowledge of either the wall thickness and index of refraction or the distance between the two light sources.

## 4.3 Determining the Unknown Properties of the Test Section and Liquid

With the dry wall reference positions known, the unknown properties of the test section or test fluid can be determined. Beginning with the simplest case, if either the index of refraction of the wall material, $n_w$, or the wall thickness, $t_w$, is known, the other value may be calculated from

$$x_{dry} = 2t_w \tan(\theta_{cw}), \tag{4.1}$$

where $\theta_{cw} = \sin^{-1}(1/n_w)$.

If, however, both $t_w$ and $n_w$ are unknown while the index of refraction of the liquid, $n_l$, is known, or $n_l$ is unknown while the other two are known, some knowledge of the light interaction with both the fluid and the wall material must be obtained.

To this point, all of the liquid measurements discussed have been concerned with the light rays completely reflected from the liquid surface. Total internal reflection occurs at the wall-liquid interface as well. Normally, the liquid films are thin enough that the reflected light from the wall-liquid interface is not detected. This is due to the fact that, for films less than a transition thickness $t_{tl}$, the critical angle of the wall-liquid interface is much greater than the angle of rays that pass through the interface and reach the liquid-vapor interface at an angle equal to or greater than its critical angle. Therefore, the percentage of light reflected from the wall-liquid interface is relatively small. Secondly, the image created by these reflected rays is obscured by the brighter image created by the rays reflecting from the surface.

The transition thickness may be derived from Figure 4.2 as follows:

$$x_{liq} = 2t_w \tan\theta_{cw} + 2t_l \tan\theta_{cl}$$

$$x_{fld} = 2t_w \tan\theta_{cwl},$$

where $\theta_{cwl}$ is the critical angle for reflected light at the wall-liquid interface. When $t_l = t_{tl}$, $x_{liq} = x_{fld}$, so, assuming a non-sloping liquid surface, setting the above equations equal and solving for $t_l$ gives,

$$t_{tl} = \frac{t_w(\tan\theta_{cwl} - \tan\theta_{cw})}{\tan\theta_{cl}} \tag{4.2}$$

If the liquid film is thicker than $t_{tl}$, the light reflected from the liquid surface returns to the outer wall surface at a distance greater than that of the light reflected from the wall-liquid interface, and the image of these rays reflected from the wall-liquid interface becomes visible. This is depicted in Figure 4.2. In operation, this places an upper bound on the thickness of liquid that can be easily measured using the image processing algorithm described previously. However, this phenomenon can be used to determine the remaining physical properties of the test materials.

From Figure 4.2,

$$x_{dry} = 2t_w \tan\theta_{cw}$$

and

$$x_{fld} = 2t_w \tan\theta_{wl}.$$

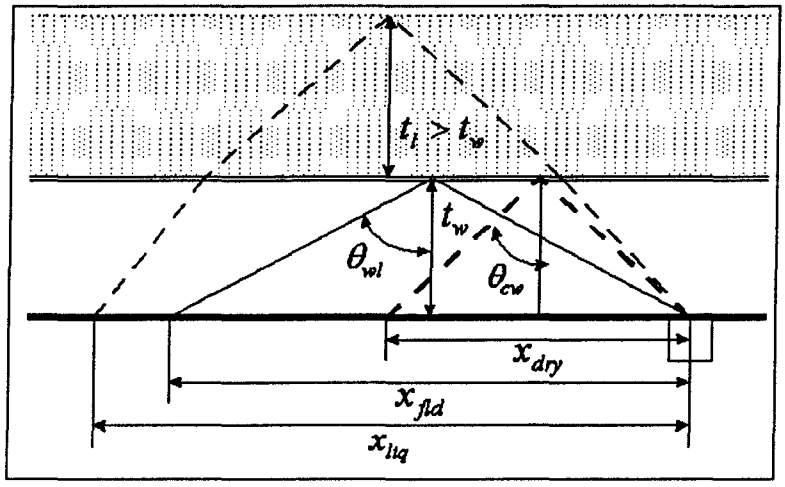


Figure 4.2: Light reflections when the liquid thickness is greater than $t_{tl}$. The reflection of light from a dry wall has been included for reference.

Subtracting $x_{dry}$ from $x_{fld}$,

$$x_{fld} - x_{dry} = 2t_w \tan\theta_{wl} - 2t_w \tan\theta_{cw},$$

or

$$x_{fld} - x_{dry} = 2t_w(\tan\theta_{wl} - \tan\theta_{cw}). \tag{4.3}$$

Now, from Snell's Law,

$$n_l \sin\theta_{lw} = n_w \sin\theta_{wl}$$

and

$$n_{vap} \sin\theta_{vw} = n_w \sin\theta_{wv},$$

where $\theta_{lw}$ is the angle from the interface normal of the light entering the liquid at the wall surface, and $\theta_{vw}$ is the angle from the interface normal of the light entering the vapor at the liquid surface.

Now, when $\theta_{wl}$ is the critical angle at the wall-liquid interface, $\theta_{cwl}$, and $\theta_{wv}$ is the critical angle for the wall/air interface, $\theta_{cw}$, $\theta_{lw} = \theta_{vw} = 90°$ and $\sin\theta_{lw} = \sin\theta_{vw} = 1$. In addition, $n_{vap} = 1.000$ so

$$n_l = n_w \sin\theta_{wl},$$

and

$$1 = n_w \sin\theta_{cw}.$$

Dividing the first equation by the second,

$$n_l = \frac{\sin \theta_{cwl}}{\sin \theta_{cw}}. \tag{4.4}$$

Equations (4.1), (4.3) and (4.4) are completely defined if the distances $x_{dry}$ and $x_{fld}$ are determined by measurement and one of the indices of refraction, $n_l$ or $n_w$, or the wall thickness, $t_w$, is known. Hence, this part of the calibration procedure requires the following basic steps:

- Obtain an image of the reflected light with a liquid layer greater than the wall thickness (greater than $t_{tl}$) in the test section (assuming the steps above for the dry wall have been completed).
- Process this image to determine $x_{fld}$, the distance between the reflected rays and the light source.
- Request input from the experimenter. At least one of the following must be given:
  - Index of refraction of the wall material
  - Index of refraction of the liquid
  - Thickness of the wall
- Solve the appropriate set of equations to determine the missing data, if any. (The experimenter may choose to enter all of the material and liquid properties.)

Solving for $t_w$ or $n_w$ from Equation (4.1) is quite simple. If Equations (4.1), (4.3) and (4.4) need to be solved simultaneously for two unknowns, however, the regula falsi method is used to numerically solve the equations. The regula falsi method is described by Scheid (1988).

## 4.4 Implementation of the Calibration Procedure

The calibration procedure is implemented in a manner designed to be convenient for the experimenter and to lessen the chance of uncertainty in the

measurements. First, the pixel scale factor must be determined. Once determined for a given set-up, it is generally unnecessary to repeat this operation. Next, the experimenter is presented with three options:

1. Perform the dry wall calibration
2. Perform the flooded wall calibration
3. Determine $t_w$, $n_l$ and $n_w$

If a completely new test section and new liquid are to be measured, each step must be performed. However, the flooded wall calibration is required only when two of the properties are unknown and need to be determined, and step 3 is only required when a new test section or liquid is used. If the properties of the new test section and fluid are known a priori, those values may be entered directly without performing the flooded wall calibration.

Experience has shown that the dry wall calibration should be performed with each new camera placement. Essentially, this serves to "zero" the measurement by defining the dry wall reflection positions. This compensates for any movement of the camera relative to the LED's that might have occurred in re-mounting the apparatus. If the wall is not of uniform thickness throughout the test section, steps 1 and 3 need to be performed at each new measurement location to adjust the value of the wall thickness, $t_w$.

Finally, this calibration procedure can be used to determine the index of refraction of any liquid that does not significantly reflect or absorb the light generated by the LED's. A test apparatus for this purpose can be constructed of a material with known wall thickness and index of refraction, and steps 2 and 3 performed to determine the test liquid's index of refraction.

# Chapter 5

# Experimental Validation and Analysis

## 5.1 The Experimental System

The components necessary for implementing this film thickness measurement system have been introduced in Section 3.5. This section details the construction of the experimental measurement system.

High brightness LED's from Radio Shack (part number 276-087) with a typical wavelength of 660 nm are used for the two light sources. These are powered from the same 12 volt power supply used by the camera. Two 150 ohm resistors in series with the LED's limit the current, though not below the suggested maximum operating current level. This was done to obtain high intensities while knowingly shortening the life of the LED's. During the course of the initial experimental work, the LED's appeared to have a limit of about 50 to 100 working hours before their intensities fell below the required level. Other LED sources may provide greater intensities at lower currents, thus enhancing component lifetimes.

The LED casings must be modified so that a point source of light may be placed at the test section wall. First, the rounded top of the LED is removed to just above the light emitting element. Then, the case is painted black except for the area immediately above the emitting element. The LED's are then mounted approximately 3 cm above the camera lens using a short piece of 1 inch schedule 40 PVC pipe.

The video camera is an inexpensive, monochrome CCD camera in 1/3

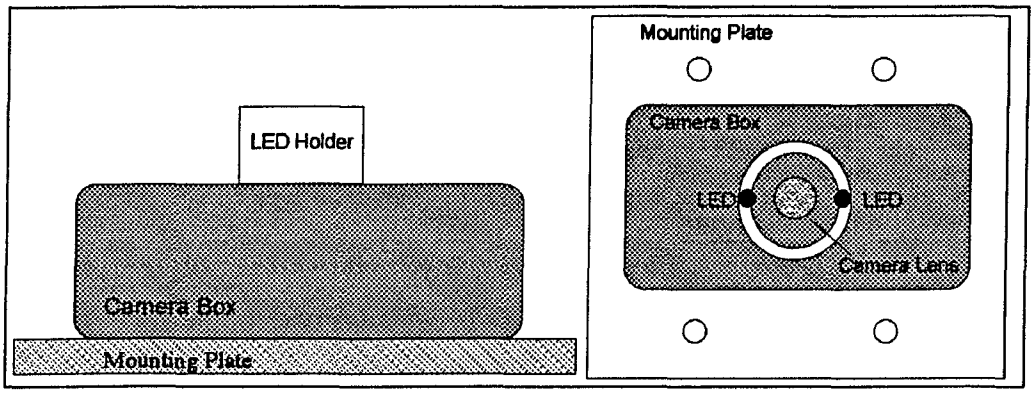


Figure 5.1: Important features of the camera assembly. Side view on the left, top view on the right.

inch format with an adjustable micro-lens. The CCD array is made up of 420 horizontal rows by 360 vertical columns of sensors. The output of this array is converted to 512 horizontal lines by 486 vertical lines by the camera electronics to generate NTSC standard interlaced output. These cameras are typically sold for surveillance or hobby applications and can be purchased quite reasonably from surplus supply companies. The camera is supplied with 12 VDC with a 600 mA wall transformer. A small plastic box with a hole in the lid just large enough for the camera and ventilation holes in its sides and back is used as a housing, with the LED holder fastened to the lid. The important features of the camera assembly are shown in Figure 5.1.

The camera box is then secured to a mounting plate with 4 holes drilled in it to allow the camera assembly to be mounted to the side of a test section. Figure 5.2 shows the camera assembly mounted to a cylindrical test section. The backside mounting support is fabricated from a 4 inch PVC coupling, cut in half, with 4 holes drilled to mate with the holes in the camera mounting base. Four bolts through these holes secure the camera to the test section. Two lengths of 1/4 inch PVC have been glued to the top center of the back support to ensure that the assembly is centered and aligned with the axis of the test section.

Video data from the camera is acquired and digitized by a Truevision Targa+ image capture card (often called a framegrabber). When processing monochrome data, the Targa+ uses 8 bits to encode the gray level informa-

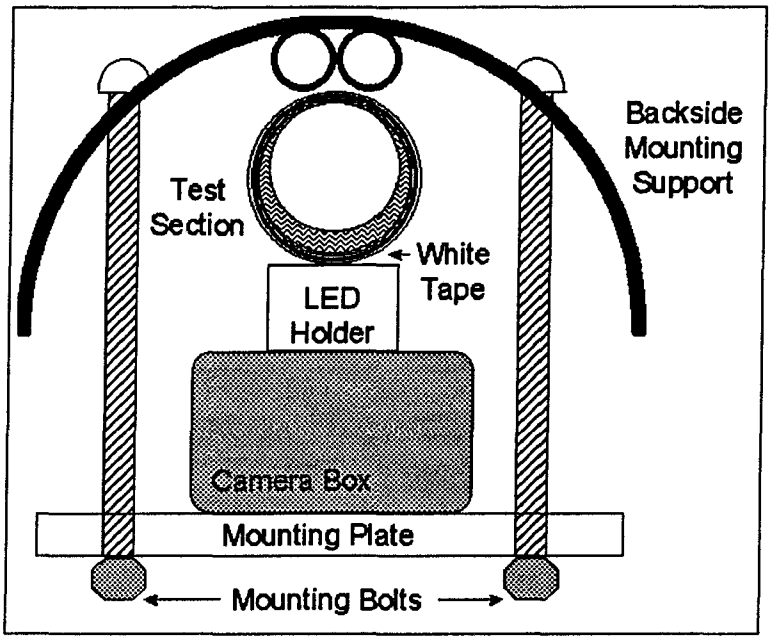


Figure 5.2: Mounting the camera assembly to a cylindrical test section.

tion in the image. Thus, each image pixel is assigned a value between 0 (no light) and 255 (maximum light intensity). An IBM-compatible computer with a 486sx microprocessor, 8 Mb of RAM and 100 Mb of hard disk storage is used to control the framegrabber and process the images.

Custom software has been written to access the framegrabber and implement the image processing algorithm described in Section 3.6. Including debug code and documenting comments, the film thickness measurement software contains over 3000 lines of C++ code. This may be compiled using the reasonably standard and freely available Gnu C++ compiler from the Free Software Foundation [1]. This software implements about 20 different image manipulation functions. The user may then create a custom image processing system for each measurement application by combining these functions. Commands may be issued via a standard input file or interactively from the keyboard.

As implemented, each image is processed in approximately 9 seconds, but

[1] As it is impractical and fairly useless to include so much code in this document, the software will be made available via the Internet. The author or advising professor may be contacted through the Mechanical and Industrial Engineering department for more information.

| Measured Width (pixels) | Measured Scale Factor | Software Width (pixels) | Software Scale Factor | Difference in Scale Factor |
|---|---|---|---|---|
| 166 | 0.0757 | 164 | 0.0766 | 1.2% |
| 173 | 0.0726 | 176 | 0.07136 | -1.7% |
| 173 | 0.0726 | 178 | 0.0706 | -2.8% |
| 179 | 0.0702 | 177 | 0.0708 | 0.9% |

Table 5.1: Verification of the pixel scale factor calibration procedure

this may be shortened to about 4 seconds if intermediate images do not need to be saved or viewed. Each image will contain an even and odd field, with each field displaying light reflected from each of the two LED's, so four measurements are actually made with each image acquisition. Data from many images may be stored and averaged together as discussed in Section 3.8.

## 5.2 Experimental Validation

Both the experimental system and the proposed film thickness measurement method must be validated. This is achieved by attempting to confirm the functionality of each system component, as well as confirming that the method generates results consistent with known data.

### 5.2.1 Calibration Parameters

#### The Pixel Scale Factor

The pixel scale factor is determined as described in Section 4.1. Verification of this measurement and calculation is performed by acquiring an image of the reference object and displaying it on a monitor. The image on the monitor is manually measured using calipers and then converted to an equivalent width in pixels. For the monitor used, 1 cm = 16 pixels. The known width of the reference object (12.56 mm) is then divided by the pixel width of the object which results in the pixel scale factor. This is then compared with the result generated by the image processing software. The results are presented in Table 5.1.

The agreement between the software and manual measurements is quite

good, especially since the caliper readings have an uncertainty of about 3% in this range. This indicates that the image processing algorithm is accurately locating the sharp change in contrast and is able to accurately and consistently determine pixel locations for the object edges.

Some variation is noted in the pixel scale factors listed in the table. The largest variations were the result of finding the pixel scale with the reference object placed lightly on top of the camera assembly, versus securing the reference object with bolts. The compression of the tape, camera box lid, and other structures brings the reference object a little closer to the camera, thus decreasing the pixel scale factor. In actual use, the camera is secured in nearly the same fashion each time it is re-mounted, so pixel scale variations are very small.

### Determination of Unknown Material Properties

The calibration procedure described in Section 4.3 will determine two of three important material parameters using measured reflections from both a dry wall and a wall with a thick layer of fluid on it.

In each of the following cases, the wall material is acrylic (methyl methacrylate) and the liquid is water. Acrylic has a refractive index of $n_w = 1.489$ in the red wavelength (ASM International Handbook Committee; 1988, p.596), while water has a refractive index of $n_l = 1.330$ (Weast; 1983, p.E-362).

In general, the data of Table 5.2 indicates that the calibration procedure works quite well. In gathering the data, it has been found that much of the error and inconsistency in the calibration results comes from the measurement of the distance between the two sources. One issue is the determination of exactly which two points should be used as the reference points on the sources. For example, an argument could be made from the paths of the light rays that the correct distance is the distance between the outside edges of the light emitting elements. However, this is difficult to verify, and did not always give consistent results. Another issue is the difficulty of physically measuring this distance, whether by using calipers to measure points on the sources or calculating the source positions by measuring distances between the reflected light rings. Finally, it seems to be fairly certain that the sources in the experimental apparatus used are not securely mounted enough to prevent slight movement

| Given | Found | Error |
|---|---|---|
| $n_l = 1.33$<br>$t_w = 3.2$ mm | $n_w = 1.50$ | 0.7% |
| $n_l = 1.33$<br>$t_w = 6.05$ mm | $n_w = 1.489$ | 0.0% |
| $n_l = 1.33$ | $n_w = 1.51$<br>$t_w = 3.235$ mm | 1.4%<br>1.1% |
| $t_w = 2.94$ mm | $n_l = 1.297$<br>$n_w = 1.460$ | -2.4%<br>-2.0% |
| $t_w = 2.94$ mm | $n_l = 1.306$<br>$n_w = 1.469$ | -1.8%<br>-1.3% |
| $n_l = 1.33$ | $n_w = 1.52$<br>$t_w = 3.17$ mm | 2.1%<br>7.8% |
| $t_w = 2.95$ mm | $n_l = 1.337$<br>$n_w = 1.503$ | 0.5%<br>1.0% |
| $t_w = 2.95$ mm | $n_l = 1.331$<br>$n_w = 1.499$ | 0.1%<br>0.7% |

Table 5.2: Using the calibration procedure to determine unknown material properties.

when the camera assembly is firmly mounted to a test section. Movements of a few tenths of a millimeter can mean significant errors in the calibration results.

To verify the use of this system with a material other than acrylic, the index of refraction of a piece of clear PVC has been calculated. The thickness of the PVC is determined to be 5.94 mm. Two separate calibration measurements generated $n_w = 1.575$ and $n_w = 1.552$. The refractive index of blue tinted clear PVC is about 1.53 (Nass; 1977, p.723), though the exact composition of the PVC is not known.

## 5.3 Film Thickness Measurements

### 5.3.1 Static Liquid Measurements

#### Measurement Procedure

Figure 5.3 shows the apparatus used to compare the measurements made using the automated optical system with those made using the needle-contact

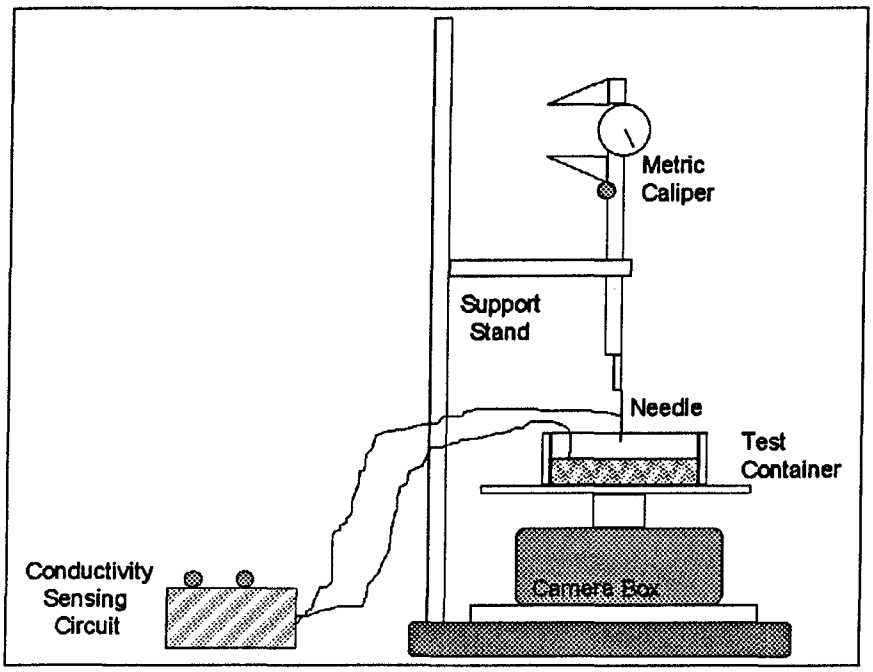


Figure 5.3: Setup for static liquid film measurements.

method. The camera assembly rests on the base of a stand and an open, shallow container is placed on the LED holder. A metric dial caliper with a needle attached is mounted from the stand above the liquid container. The needle is connected to one terminal of a conductivity sensing circuit, while the other terminal of the circuit is in contact with the water. When the needle first touches the water surface, an indicator will light. The caliper assembly can be moved to measure the film thickness at either the left or right light source positions.

After calibrating the optical system to the container wall, the measurements proceed as follows:

- Locate the left surface reflection point (about half the distance between the source and the reflected light ring).
- Lower the needle until it first comes in contact with the water. Note dial reading.
- Lower the needle until it first touches the wall. Note the reading.
- Repeat these steps 5 to 10 times.

| $t_L$ (Caliper) (mm) | $t_L$ (Optical) (mm) | Percent Difference | $t_R$ (Caliper) (mm) | $t_R$ (Optical) (mm) | Percent Difference |
|---|---|---|---|---|---|
| 1.54 | 1.52 | 1.3% | 1.63 | 1.55 | 4.9% |
| 1.15 | 1.17 | -1.7% | 1.30 | 1.22 | 6.2% |
| 0.97 | 0.97 | 0.0% | 1.00 | 0.96 | 4.0% |
| 0.79 | 0.79 | 0.0% | 0.91 | 0.86 | 5.5% |
| 0.45 | 0.56 | 25.0% | 0.67 | 0.64 | 4.5% |

Table 5.3: Static liquid film thickness measurements–Thin wall.

| $t_L$ (Caliper) (mm) | $t_L$ (Optical) (mm) | Percent Difference | $t_R$ (Caliper) (mm) | $t_R$ (Optical) (mm) | Percent Difference |
|---|---|---|---|---|---|
| 2.11 | 2.12 | -0.5% | 2.28 | 2.23 | 2.2% |
| 2.04 | 2.08 | 2.0% | 2.21 | 2.22 | 0.5% |
| 1.58 | 1.67 | 5.7% | 1.76 | 1.92 | 9.0% |
| 1.36 | 1.39 | 2.2% | 1.56 | 1.65 | 5.8% |
| 1.12 | 1.11 | -0.9% | 1.27 | 1.29 | 1.6% |
| 0.80 | 0.80 | 0.0% | 1.00 | 1.03 | 3.0% |

Table 5.4: Static liquid film thickness measurements–Thick wall.

- Repeat for the right source.
- Move caliper assembly from the container.
- Use optical system to take 50 data points from each source and average the results.

### Results

Table 5.3 presents the results for measurements taken using a thin-walled container, $t_w = 2.95$ mm. The wall thickness is determined using a micrometer with a precision of 0.0001 in. or 0.0025 mm. Table 5.4 presents the results for measurements taken using a thick-walled container, $t_w = 6.05$ mm.

During the final measurement with the thin-walled apparatus, the surface of the water was visibly deformed near the left source, possibly contributing to the large discrepancy indicated. The relatively large errors of the four data

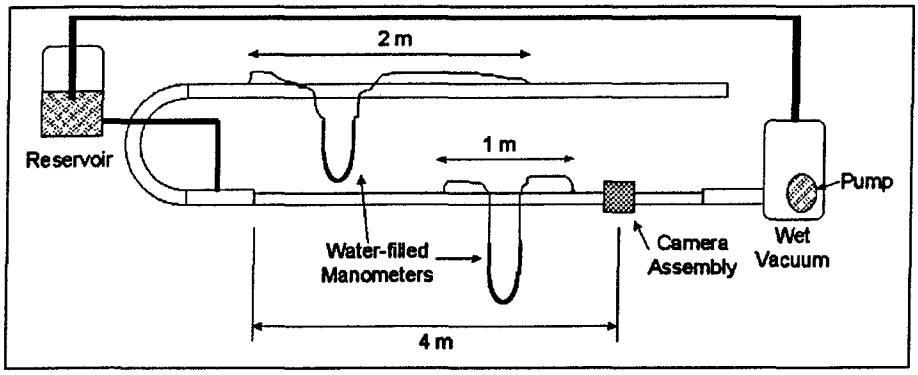


Figure 5.4: Schematic of Horizontal air-water flow loop.

points in the center of the the thick-walled data set may be attributable to the uncertainty in the caliper measurements. The caliper appears to have an uncertainty of about 0.05 mm. For the two sets of data with differences consistently greater than 2.0%, only 5 data points were taken with the caliper. At least 7 data points were taken for the remaining data in both tables.

Overall, the optically measured data agree with the contact data to within 3.9%. If the five data points that have been questioned due to possible experimental error are excluded, agreement is within 2.3%. This is within the range of the apparent uncertainty of the caliper used, and is better than much that is reported in the literature for various film measurement techniques (generally 5% to 10%). See, for example, Coney et al. (1989); Paras and Karabelas (1991); Himmelsbach et al. (1994); and Evers and Jackson (1995).

### 5.3.2 Flowing Film Measurements

#### Measurement Procedure

A horizontal air-water flow loop, depicted in Figure 5.4, has been constructed to study the liquid film distribution in horizontal, annular, two-phase flow in passages of varying sizes and geometries. The loop consists of about 7.5 m of 38.1 mm I.D. PVC pipe on the air inlet side. Pressure taps 2 m apart are connected to an inclined, water-filled manometer to give the pressure drop through this section. Water is injected circumferentially into the test section from a raised reservoir. The test section consists of about 4.9 m of 25.3 mm I.D. acrylic tubing. Pressure taps 1 m apart are connected to a vertical water-

filled manometer. The vapor flow is driven by a 6.0 HP Craftsman Wet-Vac. A sump pump in the wet-vacuum tank is actuated by a float switch to refill the reservoir.

Air flow characteristics are obtained using the pressure information from the inlet section. The pressure drop, air density and temperature can be used with relations for the Fanning friction factor, mass flow rate and Reynold's number to solve for the mass flow rate of air through the system. Liquid mass flow rates are determined by timing the fall of the liquid level in the reservoir. The measurements of mass flow rates are believed to be accurate to better than 5%.

### Results

Liquid film thickness data is measured 4 m from the beginning of the test section, about 160 L/D's. The camera assembly is mounted on the tube as shown in Figure 5.2, and 25 images are analyzed at 8 radial locations, each separated by 45°. Thus, the average of 100 measurements is used at each location to calculate the average film thickness, $h$. The measurement results are given in Figure 5.5.

Aside from the shift in the peak film thickness, the measured data follows the trends of the other researchers well. The measured flow distribution appears to be rotated about 45° from what would be expected, and no clear explanation can be given. However, it should be noted that the data presented by Fukano and Ousaka, as well as Hurlburt and Newell, only include half the cylinder and are assumed to be symmetric. Data presented by Dallman (1978) indicate some asymmetry, though he only provides one additional radial point to compare with.

Fukano and Ousaka measure significantly thinner films on the top of their test section. This is possibly explained by the fact that their test section had an inner diameter of 26 mm, versus the 25.3 mm used in this experiment, as well as by the higher air flow used in their work. In addition, Fukano and Ousaka used conductance probes to obtain their data and this measurement method may be prone to under-predicting the film thickness in thin liquid films due to the wavy surface and entrained air bubbles.

Hurlburt and Newell obtained their data using the optical technique on

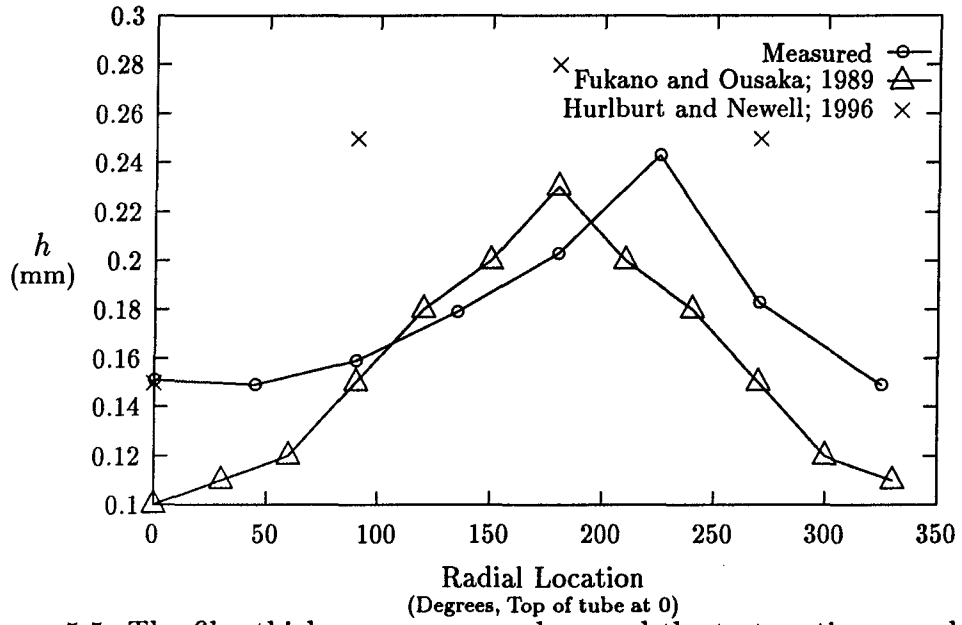


Figure 5.5: The film thicknesses measured around the test section are plotted together with representative data from the literature. The measured flow conditions are $\dot{m}_a = 0.021$ Kg/s, $\dot{m}_l = 0.019$ Kg/s. The Fukano and Ousaka data is taken from a flow with $\dot{m}_a = 0.025$ Kg/s, $\dot{m}_l = 0.019$ Kg/s. Hurlburt and Newell measured a flow with $\dot{m}_a = 0.020$ Kg/s, $\dot{m}_l = 0.013$ Kg/s.

which the current measurements are based and found thicker films in general. However, it is possible that the thicker film measurements they report can be attributed to overestimating the size of the reflected light ring, since the measurement of the ring was performed manually. Further, their data was obtained using fewer samples of the optical signal and at a location on the test section with much shorter development length. Finally, it is possible that, because of the algorithm described in Section 3.8 used to eliminate noisy optical signals, the automated system may tend to filter out thicker waves on the liquid surface, thus giving a thinner average film thickness.

## 5.4 Sensitivity Analysis

As is apparent from the discussion of the image processing algorithm in Section 3.6 and the calibration procedure in Chapter 4, the calculation of accurate film thicknesses is dependent upon many parameters. In an effort to understand how the film thickness calculation is affected by the different measured quantities, a single test case has been analyzed by varying input quantities over a known range. Similarly, the sensitivity of the calibration procedure to variations in input values has been performed. The results of these analyses are given in Appendix C.

In summary, changes of $\pm$ 5% in $n_l$ or $n_w$ will cause changes of about 10% in the film thicknesses calculated. From the calibration analysis, errors of 5% in the determination of $n_l$ or $n_w$ are possible if the measurement of $d_{src}$ or $p_{scale}$ is in error by 5% and neither $n_l$ or $n_w$ are known beforehand.

A 5% error in the knowledge of either $t_w$ or $p_{scale}$ will be reflected as about a 5% deviation in the calculated film thicknesses. Determining an unknown $t_w$ using the calibration procedure is very sensitive to almost all parameters. A 5% difference in $n_l$, $n_w$, $d_{src}$ or $p_{scale}$ will generate errors of 10% to 20% in the value of $t_w$ thus determined.

If, for some reason, the image processing algorithm for determining the position of the first fully reflected ray is off by 5 pixels, the film thicknesses calculated will be in error by about 7%. Finally, the film thickness calculations are most sensitive to changes in $d_{src}$. A 5% variation in $d_{src}$ will generate about a 15% difference in the film thickness values.

# Chapter 6

# Conclusions

## 6.1 Summary

An automated optical liquid film thickness measurement system has been presented both in theory and application. Compared with other techniques currently available for measuring thin liquid films, this optical system shows advantages in flexibility and precision. The method is not limited to a particular fluid or flow configuration, as long as a test section with transparent walls is available and the fluid does not heavily absorb or scatter the light at the wavelengths used. With a precision of about 30 microns, very thin films may be measured. In addition, using large numbers of averaged data points, films on the order of 30 microns or less may be measured with statistical confidence. This precision limit is determined primarily by the camera lens and CCD array. Greater precision may be obtained with a larger array or a lens system with greater magnification. As implemented, liquid films have been measured which agree with needle-contact measurements to within about 3%. In addition, good agreement with published data is shown for measurements of flowing films.

The implementation described uses two separate light sources. From the data collected and the sensitivity analysis that has been performed, it is recommended that future systems use a single LED, if possible, due to the errors that can be associated with uncertainties in the knowledge of the distance between the two sources. This, however, will limit the application of the method to films less than about 2 mm and test section wall thicknesses of about 4 mm or less. The dual light source system maybe used with thicker walls and films,

but care must be taken in determining the source separation.

## 6.2 Other Applications

This work has led to the development of other potential applications of the theory used for the film thickness measurement. As shown in Figure 6.1, it seems possible to derive a profile of the flowing liquid surface using the image processing techniques that have been developed. Several issues need to be resolved yet before the images can be directly correlated to the fluid surface, but it is apparent that fine structure and much qualitative information can be ascertained quite simply.

Other possible applications include the determination of liquid properties through the use of surface profiling, concentration measurement by detecting changes in index of refraction, and manufacturing process monitoring.

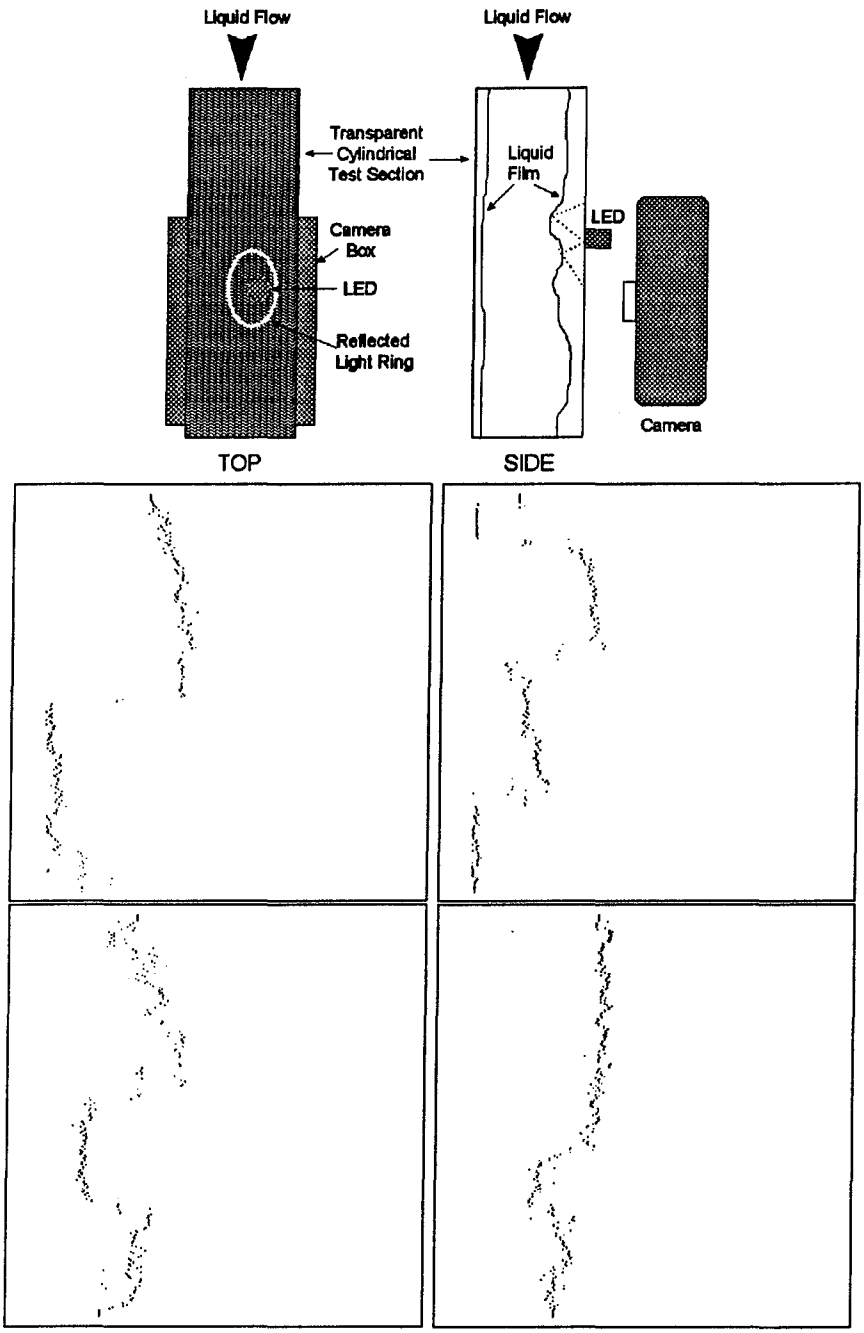


Figure 6.1: These images are the result of processing video data taken in the axial direction. The test section wall is on the left side of each image and the flow direction is from top to bottom.

# Appendix A

# The Angle at the Wall–Liquid Interface

Earlier it was emphasized that the angle with which the light ray that reflects from the liquid surface at the liquid–air critical angle approaches the wall–liquid interface is the critical angle corresponding to a wall–air interface. This can be shown with reference to Figure A.1. First, from Snell's Law,

$$n_l \sin\theta_{lw} = n_w \sin\theta_{wl}.$$

If the liquid surface is parallel to the wall surface,

$$\theta_{lw} = \theta_{cl}$$

because they are opposite interior angles of two parallel lines. Substituting,

$$n_l \sin\theta_{cl} = n_w \sin\theta_{wl}.$$

But, $\theta_{cl}$ is the critical angle for the liquid air interface, so

$$\theta_{cl} = \sin^{-1}(\frac{1}{n_l}).$$

This, then, gives

$$n_l \sin(\sin^{-1}(\frac{1}{n_l})) = n_w \sin\theta_{wl}$$

$$n_l \cdot \frac{1}{n_l} = n_w \sin\theta_w$$

$$\sin\theta_{wl} = (\frac{1}{n_w}).$$

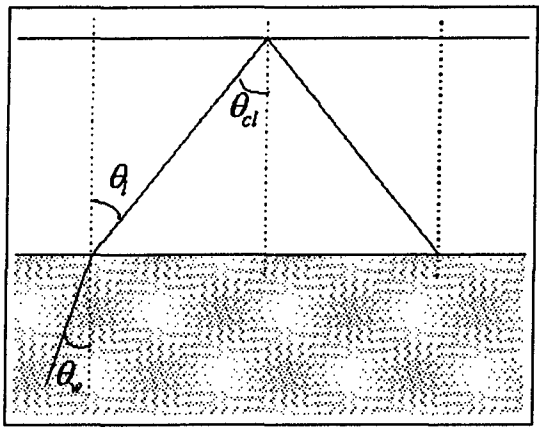


Figure A.1: Angles of the light ray that will reflect from the liquid surface at the critical angle

Since $n_{air} = 1$, this can be written

$$\sin\theta_{wl} = \frac{n_{air}}{n_w}.$$

Now, by comparison with the equation defining the critical angle, (3.2),

$$\sin\theta_c = \frac{n_2}{n_1},$$

it is evident that $\theta_{wl}$ must be equal to the critical angle at the wall–air interface, $\theta_{cw}$.

Note that this is true only for the first fully reflected light ray, which is the only light ray to reflect from the liquid–air interface at the critical angle $\theta_{cl}$.

# Appendix B

# Low Pass Filter Behavior of the Averaging Filter

The averaging operation has been described as acting as a low pass filter. This can be shown as follows. In one dimension, using the definition of the convolution sum, Equation (3.17), the averaging operation can be written as

$$P(x) = \sum_{i=-N}^{N} I(i)F(x-i) = I * F. \tag{B.1}$$

$F(x)$, the averaging filter, can be described formally as

$$F(x) = \begin{cases} 1 & \text{if } -N < x < N \\ 0 & \text{otherwise} \end{cases}.$$

The image data, $I(x)$, contains $W$ pixels, and the $*$ indicates convolution. Taking the Fourier transform of (B.1), $\widehat{P}(\Omega) = \widehat{I}(\Omega)\widehat{F}(\Omega)$, since the convolution in the spatial domain becomes multiplication in the frequency domain. $\widehat{I}(\Omega)$ is the power spectrum of the frequencies contained in the image data, while the transform of the averaging filter is given by

$$\widehat{F}(\Omega) = \frac{\sin[\Omega(N+\frac{1}{2})]}{\sin(\Omega/2)}. \tag{B.2}$$

(See, for example, Oppenheim, Willsky and Young; 1983, p 339.) The spatial frequency, $\Omega$, is given by

$$\Omega = \frac{2\pi k}{W},$$

where $W$ is the total number of pixels in the row or column being analyzed and $k$ is the index of the discrete frequency points along the transformed data.

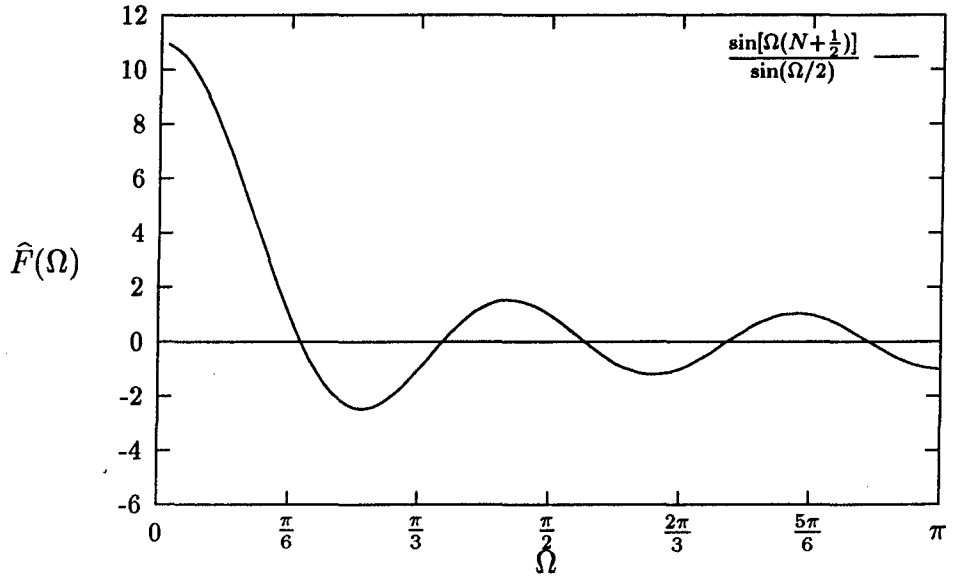


Figure B.1: The Fourier transform of the averaging filter

For instance, if $W = 500$ and $k = 20$, the corresponding frequency would be $\Omega = 0.08\pi$ radians, or 0.04 cycles/pixel. Equation (B.2) is plotted in Figure B.1. After multiplying $\widehat{F}$ and $\widehat{I}$, then, the lower frequency components of the image data will dominate and the averaging filter does indeed act as a low-pass filter.

# Appendix C

# Sensitivity Analysis Data

| | |
|---|---|
| $n_l$ | 1.330 |
| $n_w$ | 1.490 |
| $t_w$ | 2.95 mm |
| $p_{scale}$ | 0.075 mm/pixel |
| $d_{src}$ | 32.5 mm |
| $\phi$ | 0.432° |
| $t_L$ | 2.269 mm |
| $t_R$ | 2.433 mm |
| $x_r$ | 21.793 mm |

Table C.1: Base data set for measurement sensitivity analysis.

| | Base | -5% | % chg | -1% | % chg | 1% | % chg | 5% | % chg |
|---|---|---|---|---|---|---|---|---|---|
| $n_l$ | 1.330 | 1.264 | -5.000 | 1.317 | -1.000 | 1.343 | 1.000 | 1.397 | 5.000 |
| $\phi$ | 0.432 | 0.381 | -11.806 | 0.422 | -2.315 | 0.442 | 2.315 | 0.480 | 11.111 |
| $t_L$ | 2.269 | 1.998 | -11.944 | 2.216 | -2.336 | 2.320 | 2.248 | 2.522 | 11.150 |
| $t_R$ | 2.433 | 2.143 | -11.919 | 2.377 | -2.302 | 2.488 | 2.261 | 2.700 | 10.991 |
| $x_r$ | 21.793 | 21.794 | 0.005 | 21.793 | 0.000 | 21.793 | 0.000 | 21.793 | 0.000 |

Table C.2: The effect of varying $n_l$ on liquid film measurements.

| | Base | -5% | % chg | -1% | % chg | 1% | % chg | 5% | % chg |
|---|---|---|---|---|---|---|---|---|---|
| $n_w$ | 1.490 | 1.416 | -5.000 | 1.475 | -1.000 | 1.505 | 1.000 | 1.565 | 5.000 |
| $\phi$ | 0.432 | 0.433 | 0.231 | 0.433 | 0.231 | 0.433 | 0.231 | 0.432 | 0.000 |
| $t_L$ | 2.269 | 2.038 | -10.181 | 2.236 | -1.454 | 2.320 | 2.248 | 2.466 | 8.682 |
| $t_R$ | 2.433 | 2.203 | -9.453 | 2.400 | -1.356 | 2.485 | 2.137 | 2.630 | 8.097 |
| $x_r$ | 21.793 | 21.770 | -0.106 | 21.769 | -0.110 | 21.770 | -0.106 | 21.781 | -0.055 |

Table C.3: The effect of varying $n_w$ on liquid film measurements.

| | Base | -5% | % chg | -1% | % chg | 1% | % chg | 5% | % chg |
|---|---|---|---|---|---|---|---|---|---|
| $t_w$ | 2.950 | 2.803 | -5.000 | 2.921 | -1.000 | 2.980 | 1.000 | 3.098 | 5.000 |
| $\phi$ | 0.432 | 0.433 | 0.231 | 0.433 | 0.231 | 0.433 | 0.231 | 0.433 | 0.231 |
| $t_L$ | 2.269 | 2.400 | 5.773 | 2.301 | 1.410 | 2.269 | 0.000 | 2.170 | -4.363 |
| $t_R$ | 2.433 | 2.564 | 5.384 | 2.466 | 1.356 | 2.433 | 0.000 | 2.334 | -4.069 |
| $x_r$ | 21.793 | 21.760 | -0.151 | 21.772 | -0.096 | 21.740 | -0.243 | 21.751 | -0.193 |

Table C.4: The effect of varying $t_w$ on liquid film measurements.

| | Base | -5% | % chg | -1% | % chg | 1% | % chg | 5% | % chg |
|---|---|---|---|---|---|---|---|---|---|
| $d_{src}$ | 32.500 | 30.875 | -5.000 | 32.175 | -1.000 | 32.825 | 1.000 | 34.125 | 5.000 |
| $\phi$ | 0.432 | 0.450 | 4.167 | 0.435 | 0.694 | 0.430 | -0.463 | 0.417 | -3.472 |
| $t_L$ | 2.269 | 1.940 | -14.500 | 2.203 | -2.909 | 2.367 | 4.319 | 2.630 | 15.910 |
| $t_R$ | 2.433 | 2.104 | -13.522 | 2.367 | -2.713 | 2.532 | 4.069 | 2.795 | 14.879 |
| $x_r$ | 21.793 | 20.918 | -4.015 | 21.618 | -0.803 | 21.893 | 0.459 | 22.593 | 3.671 |

Table C.5: The effect of varying $d_{src}$ on liquid film measurements.

| | Base | -5% | % chg | -1% | % chg | 1% | % chg | 5% | % chg |
|---|---|---|---|---|---|---|---|---|---|
| $p_{scale}$ | 0.075 | 0.071 | -5.000 | 0.074 | -1.000 | 0.076 | 1.000 | 0.079 | 5.000 |
| $\phi$ | 0.432 | 0.416 | -3.704 | 0.430 | -0.463 | 0.436 | 0.926 | 0.450 | 4.167 |
| $t_L$ | 2.269 | 2.405 | 5.994 | 2.311 | 1.851 | 2.258 | -0.485 | 2.175 | -4.143 |
| $t_R$ | 2.433 | 2.561 | 5.261 | 2.474 | 1.685 | 2.424 | -0.370 | 2.347 | -3.535 |
| $x_r$ | 21.793 | 21.492 | -1.381 | 21.698 | -0.436 | 21.815 | 0.101 | 21.997 | 0.936 |

Table C.6: The effect of varying $p_{scale}$ on liquid film measurements.

| | Base | -5 pix. | % chg | -1 pix. | % chg | 1 pix. | % chg | 5 pix. | % chg |
|---|---|---|---|---|---|---|---|---|---|
| $p_L$ | 89 | 84 | -5 pix | 88 | -1 pix | 90 | 1 pix | 94 | 5 pix |
| $p_R$ | 236 | 241 | -5 pix | 237 | -1 pix | 235 | 1 pix | 231 | 5 pix |
| $\phi$ | 0.432 | 0.425 | -1.620 | 0.431 | -0.231 | 0.434 | 0.463 | 0.440 | 1.852 |
| $t_L$ | 2.269 | 2.104 | -7.272 | 2.236 | -1.454 | 2.301 | 1.410 | 2.433 | 7.228 |
| $t_R$ | 2.433 | 2.269 | -6.741 | 2.400 | -1.356 | 2.466 | 1.356 | 2.597 | 6.741 |
| $x_r$ | 21.793 | 22.168 | 1.721 | 21.868 | 0.344 | 21.718 | -0.344 | 21.418 | -1.721 |

Table C.7: The effect of varying the reflection pixel locations on liquid film measurements.

| | |
|---|---|
| $n_l$ | 1.330 |
| $n_w$ | 1.501 |
| $t_w$ | 2.95 mm |
| $p_{scale}$ | 0.076 mm/pixel |
| $d_{src}$ | 32.5 mm |

Table C.8: Base data set for calibration sensitivity analysis.

| | Base | -5% | % chg | -1% | % chg | 1% | % chg | 5% | % chg |
|---|---|---|---|---|---|---|---|---|---|
| $n_l$ | 1.330 | 1.264 | -5.000 | 1.317 | -1.000 | 1.343 | 1.000 | 1.397 | 5.000 |
| $n_w$ | 1.501 | 1.384 | -7.788 | 1.477 | -1.599 | 1.526 | 1.666 | 1.630 | 8.594 |
| $t_w$ | 2.950 | 2.521 | -14.542 | 2.862 | -2.983 | 3.035 | 2.881 | 3.389 | 14.881 |
| $x_{dry}$ | 5.271 | 5.269 | -0.036 | 5.266 | -0.092 | 5.266 | -0.091 | 5.266 | -0.097 |

Table C.9: The effect of varying $n_l$ on the calculation of calibration values.

| | Base | -5% | % chg | -1% | % chg | 1% | % chg | 5% | % chg |
|---|---|---|---|---|---|---|---|---|---|
| $n_w$ | 1.501 | 1.426 | -4.997 | 1.486 | -0.999 | 1.516 | 0.999 | 1.576 | 5.003 |
| $n_l$ | 1.330 | 1.288 | -3.158 | 1.322 | -0.602 | 1.338 | 0.602 | 1.370 | 3.008 |
| $t_w$ | 2.950 | 2.678 | -9.220 | 2.895 | -1.864 | 3.001 | 1.729 | 3.208 | 8.746 |
| $x_{dry}$ | 5.271 | 5.269 | -0.043 | 5.268 | -0.061 | 5.268 | -0.060 | 5.267 | -0.079 |

Table C.10: The effect of varying $n_w$ on the calculation of calibration values.

| | Base | -5% | % chg | -1% | % chg | 1% | % chg | 5% | % chg |
|---|---|---|---|---|---|---|---|---|---|
| $t_w$ | 2.950 | 2.803 | -5.000 | 2.921 | -1.000 | 2.980 | 1.000 | 3.098 | 5.000 |
| $n_l$ | 1.330 | 1.307 | -1.729 | 1.326 | -0.301 | 1.335 | 0.376 | 1.353 | 1.729 |
| $n_w$ | 1.501 | 1.460 | -2.732 | 1.493 | -0.533 | 1.510 | 0.600 | 1.544 | 2.865 |
| $x_{dry}$ | 5.271 | 5.269 | -0.034 | 5.269 | -0.040 | 5.267 | -0.075 | 5.266 | -0.090 |

Table C.11: The effect of varying $t_w$ on the calculation of calibration values.

| | Base | -5% | % chg. | -1% | % chg. | 1% | % chg. | 5% | % chg. |
|---|---|---|---|---|---|---|---|---|---|
| $p_{scale}$ | 0.076 | 0.072 | -5.000 | 0.075 | -1.000 | 0.077 | 1.000 | 0.080 | 5.000 |
| $n_l$ | 1.330 | 1.330 | 0.000 | 1.330 | 0.000 | 1.330 | 0.000 | 1.330 | 0.000 |
| $n_w$ | 1.501 | 1.549 | 3.198 | 1.510 | 0.600 | 1.493 | -0.533 | 1.462 | -2.598 |
| $t_w$ | 2.950 | 3.442 | 16.678 | 3.042 | 3.119 | 2.858 | -3.119 | 2.517 | -14.678 |
| $x_{dry}$ | 5.271 | 5.819 | 10.406 | 5.377 | 2.021 | 5.156 | -2.179 | 4.720 | -10.449 |
| $n_l$ | 1.330 | 1.307 | -1.729 | 1.325 | -0.376 | 1.335 | 0.376 | 1.354 | 1.805 |
| $n_w$ | 1.501 | 1.501 | 0.000 | 1.501 | 0.000 | 1.501 | 0.000 | 1.501 | 0.000 |
| $t_w$ | 2.950 | 3.256 | 10.373 | 3.010 | 2.034 | 2.887 | -2.136 | 2.641 | -10.475 |
| $x_{dry}$ | 5.271 | 5.818 | 10.373 | 5.378 | 2.034 | 5.158 | -2.136 | 4.719 | -10.475 |
| $n_l$ | 1.330 | 1.268 | -4.662 | 1.316 | -1.053 | 1.345 | 1.128 | 1.412 | 6.165 |
| $n_w$ | 1.501 | 1.424 | -5.130 | 1.484 | -1.133 | 1.519 | 1.199 | 1.601 | 6.662 |
| $t_w$ | 2.950 | 2.950 | 0.000 | 2.950 | 0.000 | 2.950 | 0.000 | 2.950 | 0.000 |
| $x_{dry}$ | 5.271 | 5.820 | 10.415 | 5.381 | 2.089 | 5.160 | -2.101 | 4.719 | -10.470 |

Table C.12: The effect of varying $p_{scale}$ on the calculation of calibration values first assuming a known $n_l$, next a known $n_w$, and finally, a known $t_w$.

| | Base | -5% | % chg. | -1% | % chg. | 1% | % chg. | 5% | % chg. |
|---|---|---|---|---|---|---|---|---|---|
| $d_{src}$ | 32.500 | 30.875 | -5.000 | 32.175 | -1.000 | 32.825 | 1.000 | 34.125 | 5.000 |
| $n_l$ | 1.330 | 1.330 | 0.000 | 1.330 | 0.000 | 1.330 | 0.000 | 1.330 | 0.000 |
| $n_w$ | 1.501 | 1.460 | -2.732 | 1.492 | -0.600 | 1.510 | 0.600 | 1.547 | 3.065 |
| $t_w$ | 2.950 | 2.370 | -19.661 | 2.828 | -4.136 | 3.071 | 4.102 | 3.588 | 21.627 |
| $x_{dry}$ | 5.271 | 4.456 | -15.461 | 5.108 | -3.088 | 5.429 | 2.994 | 6.080 | 15.345 |
| $n_l$ | 1.330 | 1.355 | 1.880 | 1.335 | 0.376 | 1.325 | -0.376 | 1.308 | -1.654 |
| $n_w$ | 1.501 | 1.501 | 0.000 | 1.501 | 0.000 | 1.501 | 0.000 | 1.501 | 0.000 |
| $t_w$ | 2.950 | 2.494 | -15.458 | 2.857 | -3.153 | 3.053 | 3.492 | 3.403 | 15.356 |
| $x_{dry}$ | 5.271 | 4.456 | -15.458 | 5.105 | -3.153 | 5.455 | 3.492 | 6.080 | 15.356 |
| $n_l$ | 1.330 | 1.445 | 8.647 | 1.350 | 1.504 | 1.312 | -1.353 | 1.252 | -5.865 |
| $n_w$ | 1.501 | 1.659 | 10.526 | 1.528 | 1.799 | 1.477 | -1.599 | 1.393 | -7.195 |
| $t_w$ | 2.950 | 2.950 | 0.000 | 2.950 | 0.000 | 2.950 | 0.000 | 2.950 | 0.000 |
| $x_{dry}$ | 5.271 | 4.457 | -15.438 | 5.107 | -3.112 | 5.428 | 2.980 | 6.084 | 15.427 |

Table C.13: The effect of varying $d_{src}$ on the calculation of calibration values first assuming a known $n_l$, next a known $n_w$, and finally, a known $t_w$.

# Bibliography


Andritsos, N. (1985). *Effect of Pipe Diameter and Liquid Viscosity on Horizontal Stratified Flow*, PhD thesis, University of Illinois at Urbana-Champaign, Urbana, IL.

ASM International Handbook Committee (1988). *Engineering Plastics*, Vol. 2 of *Engineering Materials Handbook*, ASM International, Metals Park, OH.

Azzopardi, B. J. (1986). Disturbance wave frequencies, velocities and spacing in vertical annular two-phase flow, *Nuclear Engineering and Design* **92**(2): 121–133.

Barter, J. D. and Lee, P. H. Y. (1994). Real-time wave-amplitude spectrum analyzer for air-liquid interfaces, *Applied Physics Letters* **64**(15): 1896–1898.

Bousman, W. S., McQuillen, J. B. and Witte, L. C. (1996). Gas-liquid flow patterns in microgravity: Effects of tube diameter, liquid viscosity and surface tension, *International Journal of Multiphase Flow* **22**(6): 1035–1053.

Brown, R. C., Andruessi, P. and Zanelli, S. (1978). The use of wire probes for the measurement of liquid film thickness in annular gas-liquid flows, *The Canadian Journal of Chemical Engineering* **56**: 754 – 757.

Chen, X., Butler, T. and Brill, J. P. (1996). Capacitance probes for measurement of liquid film thickness, *HTD-Vol 334, Proceedings of the ASME Heat Transfer Division at the International Mechanical Engineering Congress and Exposition*, Vol. 3, ASME, Atlanta, GA, pp. 201–208.

Chun, M.-H. and Sung, C.-K. (1986). Parametric effects on the void fraction measurement by capacitance transducers, *International Journal of Multiphase Flow* **12**(4): 627–640.

Coney, J. E. R., El-Shafei, E. A. M. and Sheppard, C. G. W. (1989). A dual laser beam method for wavy film thickness measurement, *Optics and Lasers in Engineering* **11**: 1–14.

Coney, M. W. E. (1973). The theory and application of conductance probes for the measurement of liquid film thickness in two phase flow, *Journal of Physics E: Scientific Instruments* **6**: 903 – 910.

Crane, R. (1997). *A simplified approach to image processing*, first edn, Prentice Hall PTR, Upper Saddle River, NJ.

Dallman, J. C. (1978). *Investigation of Separated Flow Model in Annular Gas-Liquid Two-Phase Flows*, PhD thesis, University of Illinois at Urbana-Champaign, Urbana, IL.

Driscoll, D. I., Schmitt, R. L. and Stevenson, W. H. (1992). Thin flowing liquid film thickness measurement by laser induced fluorescence, *Transactions of the ASME: Journal of Fluids Engineering* **114**(1): 107–112.

Evers, L. W. and Jackson, K. J. (1995). Liquid film thickness measurements by means of internally reflected light, *Electronic Engine Controls 1995*, Vol. SP-1082 of *SAE Technical Paper Series*, Society of Automotive Engineers, pp. 1–7. Reprint, number 950002.

Fukano, T. and Ousaka, A. (1989). Prediction of the circumferential distribution of film thickness in horizontal and near-horizontal gas-liquid annular flows, *International Journal of Multiphase Flow* **15**(3): 403–419.

Gonzalez, R. C. and Woods, R. E. (1992). *Digital Image Processing*, third edn, Addison-Wesley, Reading, MA.

Hagiwara, Y., Esmaeilzadeh, E., Tsutsui, H. and Suzuki, K. (1989). Simultaneous measurement of liquid film thickness, wall shear stress and gas flow turbulence of horizontal wavy two-phase flow, *International Journal of Multiphase Flow* **15**(3): 421–431.

Hagiwara, Y., Suzuki, K. and Sato, T. (1982). Studies on thin liquid film of annular-mist two-phase flow I. wave characteristics and heat transfer, *Memoirs of the Faculty of Engineering, Kyoto University* **44**: 309–328.

Hewitt, G. F. (1982). Measurement of liquid-film thickness, *in* G. Hetsroni (ed.), *Handbook of Multiphase Systems*, McGraw–Hill, New York, pp. 10–67 – 10–85.

Hewitt, G. F., Jayanti, S. and Hope, C. B. (1990). Structure of thin liquid films in gas–liquid horizontal flow, *International Journal of Multiphase Flow* **16**(6): 951–957.

Himmelsbach, J., Noll, B. and Wittig, S. (1994). Experimental and numerical studies of evaporating wavy fuel films in turbulent air flow, *International Journal of Heat and Mass Transfer* **37**(8): 1217–1226.

Hurlburt, E. T. and Newell, T. A. (1996). Optical measurement of liquid film thickness and wave velocity in liquid film flows, *Experiments in Fluids* **21**(5): 357–362.

Jayanti, S., Hewitt, G. F. and White, S. P. (1990). Time-dependent behavior of the liquid film in horizontal annular flow, *International Journal of Multiphase Flow* **16**(6): 1097–1116.

Karapantsios, T. D., Paras, S. V. and Karabelas, A. J. (1989). Statistical characteristics of free falling films at high Reynolds numbers, *International Journal of Multiphase Flow* **15**(1): 1 – 21.

Klausner, J. F., Zeng, L. Z. and Bernhard, D. M. (1992). Development of a film thickness probe using capacitance for asymmetrical two-phase flow with heat addition, *Review of Scientific Instruments* **63**(5): 3147 – 3152.

Klug, F. and Mayinger, F. (1994). Impedance based flow reconstruction-a novel flow composition measuring technique for multi-phase-flows, *Nuclear Engineering Design* **146**: 35 – 42.

Laurinat, J. E. (1979). *Pressure drop and film height measurements for annular two-phase flow in a horizontal two-inch pipe*, Master's thesis, University of Illinois at Urbana-Champaign, Urbana, IL.

Laurinat, J. E. (1982). *Studies on the Effects of Pipe Size on Horizontal Annular Two-Phase Flows*, PhD thesis, University of Illinois at Urbana-Champaign, Urbana, IL.

Maerfat, M., Akamatsu, T., Fujikawa, S., Goto, T. and Mizutani, T. (1989). An experimental study of non-equilibrium vapour condensation in a shock-tube, *Experiments in Fluids* **7**: 513–520.

Miya, M. (1970). *Properties of Roll Waves*, PhD thesis, University of Illinois at Urbana-Champaign, Urbana, IL.

Müller, H., Bellmann, H., Himmelsbach, J., Elsäßer, A., Samenfink, W. and Hallman, M. (1994). Mixture preparation and wall film behavior in suction pipes of si-engines, *MTZ: Motortechnische Zeitschrift* **55**(4): 220–226.

Nass, L. I. (ed.) (1977). *Encyclopedia of PVC*, Vol. 2, Marcel Dekker, Inc., New York.

Oppenheim, A. V., Willsky, A. S. and Young, I. T. (1983). *Signals and Systems*, first edn, Prentice-Hall, Inc., Englewood Cliffs, NJ.

Özgü, M. R. and Chen, J. C. (1973). A capacitance method of measurement of film thickness in two-phase flow, *Review of Scientific Instruments* **44**(12).

Paras, S. V. and Karabelas, A. J. (1991). Properties of the liquid layer in horizontal annular flow, *International Journal of Multiphase Flow* **17**(4): 439–454.

Pedrotti, F. L. and Pedrotti, L. S. (1993). *Introduction to Optics*, 2nd edn, Prentice Hall, Englewood Cliffs, New Jersey.

Roy, R. P., Ku, J., Kaufman, I. and Shukla, J. (1986). Microwave method for measurement of liquid film thickness in gas-liquid flow, *Review of Scientific Instruments* **57**(5): 952 – 956.

Russ, J. C. (1994). *The Image Processing Handbook*, CRC Press, Boca Raton, FL.

Sattelmayer, T., Sill, K. H. and Wittig, S. (1987). Nonintrusive optical measurement technique for wavy liquid films, *Technisches Messen* **54**(4): 155–160.

Scheid, F. (1988). *Numerical Analysis*, Schaum's Outline Series, 2nd edn, McGraw Hill, Inc., New York.

Schmitt, R. L., Stevenson, W. H. and Stevenson, H. C. (1982). Optical measurement of liquid film thickness, *Proceedings of the Inspections, Measurement and Control Symposium, International Congress of Applications of Lasers and Electro-Optics 1982*, Vol. 33, Laser Institute of America (LIA), LIA, Boston, MA, pp. 31–35.

Sekoguchi, K., Fukui, H., Matsuoka, T. and Nishikawa, K. (1975). Investigation into the statistical characteristics of bubbles in two-phase flow, *Bulletin of the JSME* **18**(118): 391 – 396.

Sekoguchi, K., Ousaka, A., Fukano, T. and Morimoto, T. (1982). Air-water annular two-phase flow in a horizontal tube, *Bulletin of the JSME* **25**(208): 1559–1566.

Sun, R. K., Kolbe, W. F., Leskovar, B. and Turko, B. T. (1981). Measurement of thickness of thin water film in two-phase flow by capacitance method, *IEEE Transactions on Nuclear Science* **NS-29**(1): 688–694.

Sundaram, R. K., Chen, J. C., London, E. J. and Eberhardt, N. (1981). Measurement of thin film thicknesses in two-phase flow, *Proceedings of the 27th International Instrumentation Symposium*, ISA Aerospace Industry Division and ISA Test Measurement Division, pp. 299–312.

Than, C. F., Tee, K. C., Low, K. S. and Tso, C. P. (1993). Optical measurement of slope, thickness and velocity in liquid film flow, *Smart Material Structures* **2**(1): 13–21.

Thorncroft, G. E. and Klausner, J. F. (1997). A capacitance sensor for two-phase liquid film thickness measurements in a square duct, *Transactions of the ASME: Journal of Fluids Engineering* **119**(1): 164–169.

Turko, B. T., Kolbe, W. F., Leskovar, B. and Sun, R. K. (1981). Development of electro-optical instrumentation for reactor safety studies, *IEEE Transactions on Nuclear Science* **NS-28**(1): 728–739.

Villeneuve, J. P. and Ouellet, Y. (1978). Laboratory systems for measuring short-term changes in water levels, *Review of Scientific Instruments* **49**(10): 1425–1431.

Weast, R. C. (ed.) (1983). *CRC Handbook of Chemistry and Physics*, 64th edn, CRC Press, Inc., Boca Raton, Florida.

Yu, S. C. M., Tso, C. P. and Liew, R. (1996). Analysis of thin film thickness determination in two-phase flow using a multifiber optical sensor, *Applied Mathematical Modelling* **20**(7): 540–548.